

Anomalous Pseudocapacitive Behavior of a Nanostructured, Mixed-Valent Manganese Oxide Film for Electrical Energy Storage

Min-Kyu Song,^{†,#} Shuang Cheng,^{†,#} Haiyan Chen,[‡] Wentao Qin,[†] Kyung-Wan Nam,[§] Shucheng Xu,^{||} Xiao-Qing Yang,[§] Angelo Bongiorno,^{||} Jangsoo Lee,[⊥] Jianming Bai,[¶] Trevor A. Tyson,[‡] Jaephil Cho,[⊥] and Meilin Liu^{*,†,#}

[†]School of Materials Science and Engineering, Center for Innovative Fuel Cell and Battery Technologies, Georgia Institute of Technology, 771 Ferst Drive, Atlanta, Georgia 30332-0245, United States

[‡]Department of Physics, New Jersey Institute of Technology, Newark, New Jersey 07102, United States

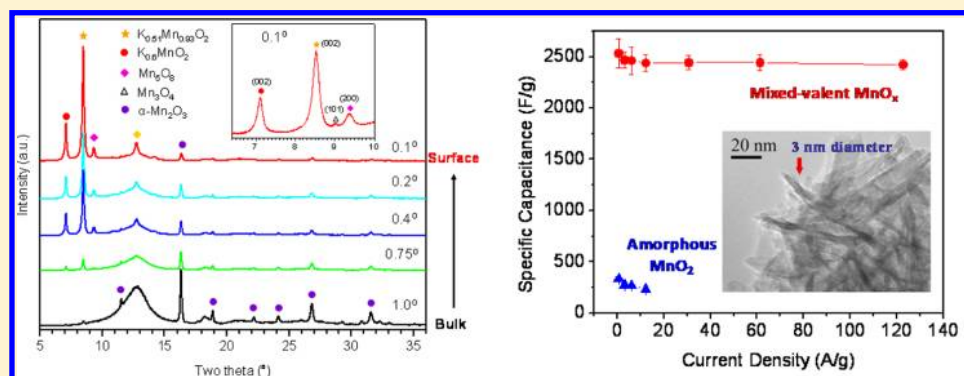
[§]Chemistry Department, Brookhaven National Laboratory, Upton, New York 11973, United States

^{||}School of Chemistry and Biochemistry, Georgia Institute of Technology, 901 Atlantic Drive, Atlanta, Georgia 30332-0400, United States

[⊥]Interdisciplinary School of Green Energy, Ulsan National Institute of Science & Technology (UNIST), 701-11,100 Banyeon-ri, Eonyang-eup, Ulju-gun, Ulsan, Korea, 689-798

[¶]High Temperature Materials Laboratory, Oak Ridge National Laboratory, Oak Ridge, Tennessee 37831, United States

Supporting Information



ABSTRACT: While pseudocapacitors represent a promising option for electrical energy storage, the performance of the existing ones must be dramatically enhanced to meet today's ever-increasing demands for many emerging applications. Here we report a nanostructured, mixed-valent manganese oxide film that exhibits anomalously high specific capacitance (~ 2530 F/g of manganese oxide, measured at 0.61 A/g in a two-electrode configuration with loading of active materials ~ 0.16 mg/cm²) while maintaining excellent power density and cycling life. The dramatic performance enhancement is attributed to its unique mixed-valence state with porous nanoarchitecture, which may facilitate rapid mass transport and enhance surface double-layer capacitance, while promoting facile redox reactions associated with charge storage by both Mn and O sites, as suggested by in situ X-ray absorption spectroscopy (XAS) and density functional theory calculations. The new charge storage mechanisms (in addition to redox reactions of cations) may offer critical insights to rational design of a new-generation energy storage devices.

KEYWORDS: Energy storage, electrochemical capacitors, mixed-valent compounds, enhanced pseudocapacitance, in situ X-ray absorption spectroscopy

While the application of existing batteries is often limited by low power, short cycle life, and long charging time,¹ the use of conventional capacitors suffers from inadequate energy density. Pseudocapacitors may bridge the gap between batteries and capacitors.² Unlike electrochemical double layer capacitors (EDLCs), which store electrical energy by accumulation of ions on electrode surface,³ pseudocapacitors make use of fast redox reactions or phase changes on the surface or subsurface of electrodes,^{4–6} offering much higher

energy densities than EDLCs. However, the rate capability and cycling stability of pseudocapacitors are perceived to be inferior to those of EDLCs and the energy density to be much lower than those of available batteries. To overcome these limitations, considerable efforts have been devoted to the creation of new

Received: March 12, 2012

Revised: June 3, 2012

Published: June 10, 2012

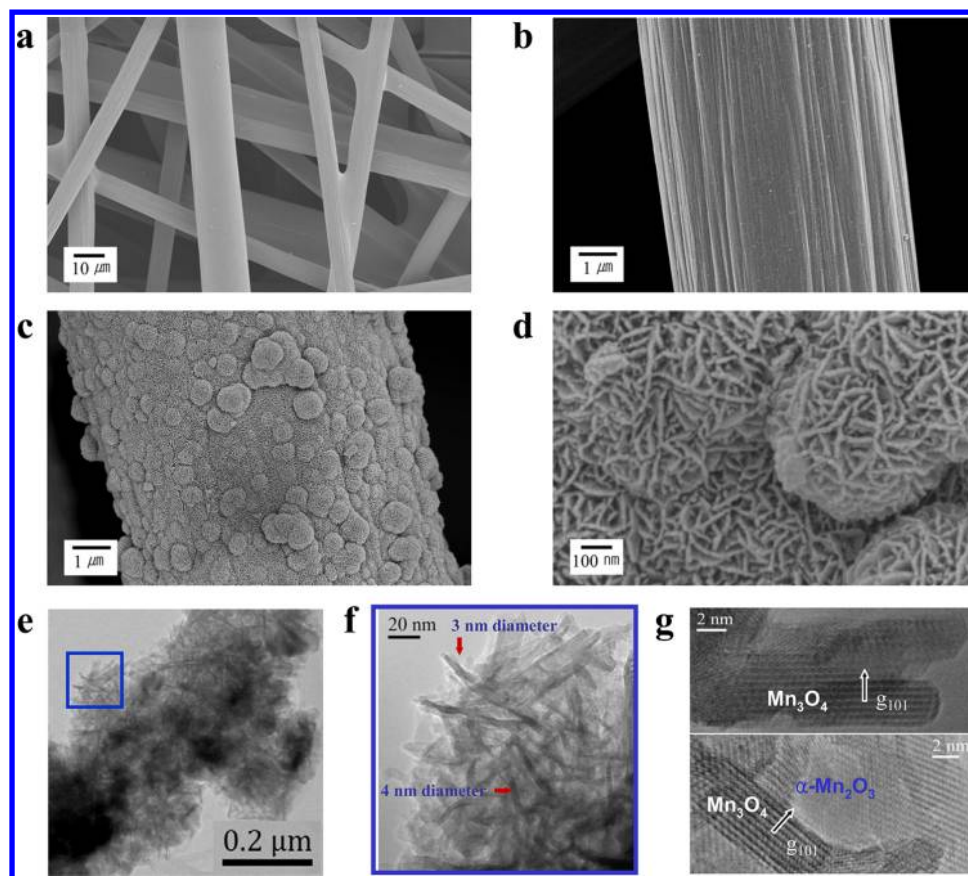


Figure 1. Electron microscopy analysis. (a) SEM image of carbon fiber paper (CFP) before coating showing 3D interconnected, porous structures. (b) SEM image of a carbon fiber before coating. (c) SEM image of a carbon fiber after conformal coating of MnO_x for 30 min. (d) SEM image of the MnO_x coating annealed at 400 °C in air for 2 h. (e) TEM image of MnO_x coating annealed at 400 °C in air for 2 h. (f) A zoomed-in view of the blue square area in (e) showing a cluster of the needle-shaped crystals with diameters of ~ 3 to ~ 4 nm. (g) High-resolution TEM images showing the fringes of Mn_3O_4 and $\alpha\text{-Mn}_2\text{O}_3$ phase.

materials for pseudocapacitors. To date, however, the progress has been hindered largely by the lack of a profound understanding of the complex charge storage mechanisms related to intercalation of ions into electrode materials (of layered or channeled structures), reaction of ions with active electrode materials (to form new phases), and/or electrochemical adsorption of ions on electrode surfaces. It is traditionally believed that the pseudocapacitive behavior is associated primarily with the redox reactions of the cations (or changes in oxidation states of the cations) in electrode materials during operation.² A suitable electrode material for high performance should promote fast, reversible redox reactions on the surface or subsurface.^{4,5}

Among many materials investigated, since first reported by Goodenough group,⁷ MnO_2 has attracted much attention because it is abundant, inexpensive, and environmentally benign. While MnO_2 has high theoretical capacitance⁸ (~ 1370 F/g as the oxidation state of Mn ion is changed from 4+ to 3+ over a potential window of 0.8 V), its poor electronic conductivity often limits the electrode utilization; only the surface layers may participate in redox reactions. To overcome this limitation, MnO_2 has been mixed with carbon particles or loaded onto carbon supports (including carbon nanotubes and graphene).^{9–16} To date, however, the reported specific capacitance of MnO_2 varies from ~ 150 to ~ 940 F/g while the cycling stability still needs further improvement. Although higher specific capacitance (~ 1145 F/g) has been

reported,¹⁷ the MnO_2 was deposited into a nanoporous gold film (~ 100 nm thick) and thus could be less competitive economically for practical applications. Further, the rate capability is still unsatisfactory for large-scale applications such as auxiliary power units for electric vehicles. With several oxidation states and a wide range of phases, manganese is a vital component in photosynthetic systems due to its unique ability to cycle between various oxidation states.¹⁸ In particular, manganese oxides can assume many different crystal structures upon accommodation of other metal cations. These complex features often give rise to unusual properties of manganese oxide. For example, the dramatic enhancement of catalytic activities toward oxidation of various organic compounds was attributed to the mixed-valence of manganese oxides.^{19,20}

The investigation of mixed-valent compounds has a long and interesting history. Mixed-valent compounds contain donor and acceptor sites separated by a bridge. Since Prussian blue, a complex Fe(II)/Fe(III) cyanide, was first discovered in 1704, the study of mixed-valent compounds has had significant impacts in chemistry, physics, and biology. In particular, from the late 1960s, molecular mixed-valent compounds began to receive great attention due to their unique optical properties arising from significant electron transitions between donor and acceptor sites by absorbing specific wavelengths of visible light via intervalence charge transfer. The intense blue color of Prussian blue is related to the energy of the electron transfer from Fe(II) to Fe(III) . Two key factors (and their interaction)

that determine their unique properties are the “electronic coupling” between the two redox sites, and the “reorganization energy” associated with electron transfer between them.²¹ Charge localization or delocalization has been a central issue in mixed-valence chemistry. By a classification scheme proposed by Robin and Day,²² mixed-valent compounds can be completely localized, fully delocalized, or systems in between, depending on the strength of the electron interaction between the oxidized and reduced sites. To date, compounds of group 8–11 transition metals have been most intensively studied. In particular, compounds of iron, ruthenium, platinum, and copper have been widely studied.²³ For example, many mixed-valent copper-based oxides have been developed as superconductors. The compound $\text{YBa}_2\text{Cu}_3\text{O}_7$ has mixed-valent Cu(II) and Cu(III). Also, a number of rare-earth compounds with atomic-like *f* levels coexisting with wide *s*–*d* band at the Fermi level have shown very unique thermal and magnetic properties.²⁴

However, the nature of the mixed-valent chemistry on the surface of nanostructured materials has not yet been fully understood and a fundamental understanding of the relationship between mixed-valent structure and properties is still lacking. It should be also noted that the mixed-valence chemistry of the early transition metals is considerably less well established, yet a remarkable variety of structurally diverse mixed-valence compounds can be formed from these elements. Their wide range of oxidation states, coordination numbers, and geometries can offer great potential for the formation of unique mixed-valent compounds, and many of these may exhibit distinctive bonding, chemistry, and properties suitable for various applications. In particular, although early transition elements such as titanium, vanadium, and manganese are important in biology, catalysis, artificial photosynthesis, and energy storage/conversion science, the controlled synthesis of their mixed-valent compounds and their unique electrochemical properties have not yet been explored. In this paper, we demonstrated the controlled synthesis of nanostructured, mixed-valent manganese oxides and explored their unique properties as electrodes for high-performance pseudocapacitors.

We used conductive and porous carbon fiber paper (CFP) as both the current collector and the electrode for conformal coating of mixed-valence MnO_x as the active electrode material for pseudocapacitors (Figure 1a,b). Individual carbon fibers in the CFP are well-connected and the pores are sufficiently large to allow efficient ion access to all surface area of the electrode. We deposited a thin, uniform coating of nanoporous MnO_x directly onto porous CFP using a simple precipitation method in an aqueous solution at 75 °C (Figure 1c,d). The porous network structure of the CFP is retained because the conformal MnO_x coating is relatively thin, as revealed by microscopy. The MnO_x coated CFP were then heat-treated at 200–450 °C in different atmospheres (air, N_2 , and 4% H_2). TEM analysis of the samples annealed at 400 °C in air for 2 h revealed that the MnO_x films consist of many low aspect-ratio crystals (each being a few tens of nanometers in size) as well as clustered and needle-shaped crystals, whose diameters vary from a few nanometers to ~10 nm (Figure 1e–g, Supporting Information S1). Selected area electron diffraction (SAED) analysis (Supporting Information Figure S1b) suggested that the low-aspect ratio nanocrystals examined are $\alpha\text{-Mn}_2\text{O}_3$ with a lattice constant of 0.94 nm, and the needle-shaped crystals were identified as Mn_3O_4 (Hausmannite) based on lattice images (Figure 1g). The lattice fringes reveal the axes of the two

needle-shaped Mn_3O_4 crystals are parallel to the (101) lattice planes (Supporting Information Figure S1c). Since both the (101) and (011) spacing are the largest lattice spacing in the Mn_3O_4 lattice, such an orientation may facilitate the incorporation and transport of ions along this direction. The thickness of MnO_x coating varied from ~70 to ~800 nm (Supporting Information Figure S2–S4), depending on the deposition time (2 to 30 min).

To further characterize the structural features of the MnO_x coatings formed on CFP, we used both laboratory and synchrotron-based X-ray diffraction (XRD) analysis. Figure 2a

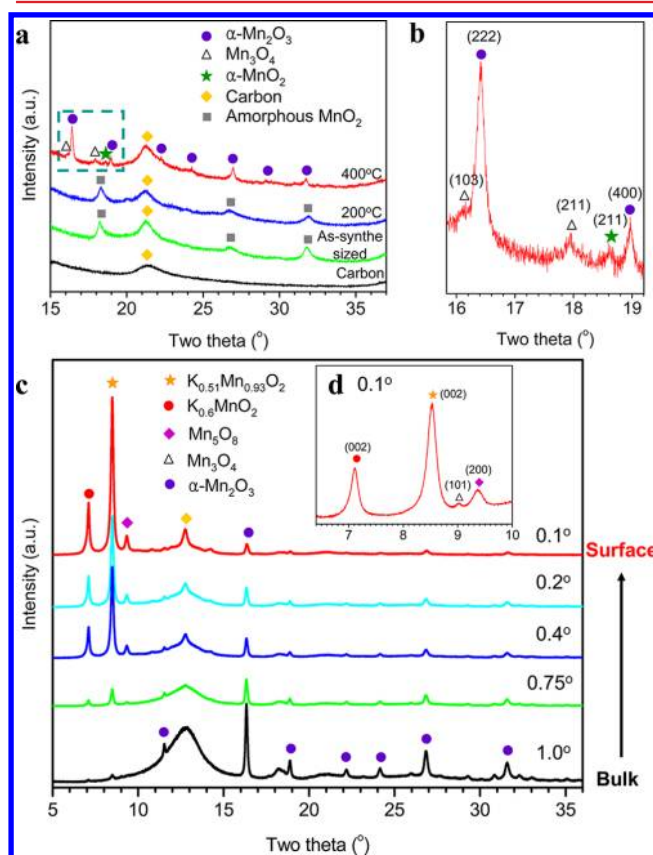


Figure 2. Synchrotron XRD analysis. (a) Transmission mode XRD pattern: bare carbon paper before coating, MnO_x electrodes before and after annealing at different temperatures (200 and 400 °C) in air for 2 h. (b) Enlarged view of XRD pattern between 16–19° of XRD pattern of MnO_x annealed at 400 °C in air for 2 h and highlighted in Figure 2a. (c) XRD pattern at of MnO_x annealed at 400 °C in air for 2 h measured at different incident angle (0.1–1°). (d) XRD pattern at incident glancing angle of 0.1° of MnO_x annealed at 400 °C in air for 2 h showing the representative surface species.

shows the synchrotron-based XRD patterns (transmission mode) of samples (deposited for 30 min) before and after annealing in air at different temperatures. The very broad characteristic peaks in the XRD patterns indicated that the as-deposited MnO_2 coating was amorphous and remained so after annealing at 200 °C in air for 2 h, which is consistent with previous studies under similar synthesis conditions.^{25,26} The amorphous phase of MnO_2 was believed to be good electrode materials for pseudocapacitors.^{7,26,27} When annealed with CFP at 400 °C in air for 2 h, the amorphous MnO_2 was converted to crystalline $\alpha\text{-Mn}_2\text{O}_3$ with small amount of Mn_3O_4 (Hausmannite) and $\alpha\text{-MnO}_2$, as evident from the XRD patterns shown in

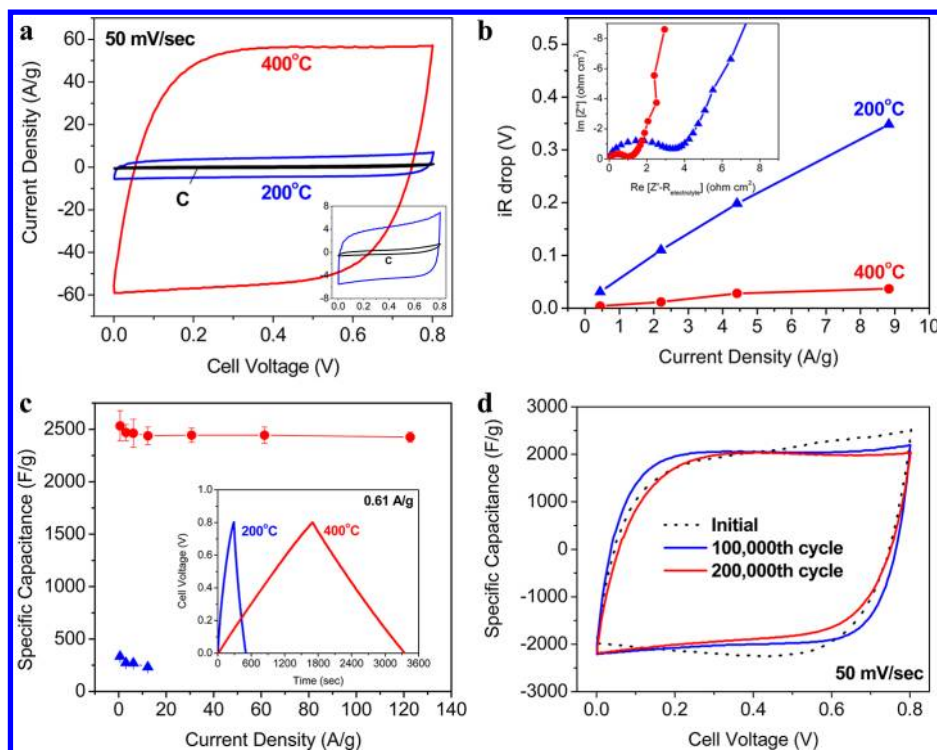


Figure 3. Electrochemical performance of symmetric pseudocapacitors constructed from amorphous MnO_2 and mixed-valent MnO_x electrodes. (a) Cyclic voltammograms measured between 0–0.8 V at a scan rate of 50 mV/s. (b) iR drop of the cells measured at different current densities. Insert shows electrochemical impedance spectra collected at open circuit voltage under the influence of an ac voltage of 10 mV. (c) Specific capacitance at different current densities demonstrating superior rate-capability. Insert shows typical charge–discharge curves of amorphous MnO_2 and mixed-valent MnO_x electrodes at a constant current density of 0.61 A/g. Only the weight of the active electrode material (MnO_x , ~ 0.32 mg) was considered in the specific capacitance calculations. (d) Cyclic voltammograms before and after long-term cycling at a scan rate of 50 mV/s showing excellent cycling stability.

Figure 2a,b. These crystalline phases started to appear at ~ 360 °C when the temperature was raised from 200 to 400 °C in air, as revealed by the in situ XRD analysis (Supporting Information Figure S5). It is noted, however, that the transmission-mode XRD pattern is quite different from those collected at a small glancing angle (Supporting Information Figure S6), suggesting that the phases on the surface are very different from those in the bulk.

To gain some insights into the structures of the surface layer, we collected XRD patterns at different glancing incident angles (Figure 2c,d). A lower incident angle corresponds to a shallower penetration depth of the X-ray, allowing us to probe the structure of a layer closer to the surface. When the incident angle was varied from 1 to 0.1°, the $\alpha\text{-Mn}_2\text{O}_3$ peaks decreased gradually while the peaks corresponding to K-incorporated MnO_2 ($\text{K}_{0.6}\text{MnO}_2$ and $\text{K}_{0.51}\text{Mn}_{0.93}\text{O}_2$) and Mn_3O_8 increased considerably, suggesting that $\alpha\text{-Mn}_2\text{O}_3$ is present predominantly in the bulk whereas the K-incorporated MnO_2 and Mn_3O_8 are formed mostly near the surface (Figure 2d). It is noted that small peaks corresponding to Mn_3O_4 were observable in both transmission-mode and glancing angle mode XRD patterns, implying that small amount of Mn_3O_4 is present in the bulk and on the surface. This is consistent with TEM observation (Figure 1g). The surface phases (K-incorporated MnO_2 , Mn_3O_8 , and Mn_3O_4) were formed at 400 °C, as indicated by the low glancing angle XRD analysis at different temperatures (Supporting Information Figure S7).

XRD analysis of the mixed-valent MnO_x of different thicknesses suggests that the predominating phase of the ~ 800 nm films (deposited for 30 min) was $\alpha\text{-Mn}_2\text{O}_3$ whereas

that of the ~ 70 nm films (deposited for 2 min) was Mn_3O_4 , which showed the highest specific capacitance. As the thickness was reduced (Supporting Information Figure S8), the predominating “bulk” phase was changed from $\alpha\text{-Mn}_2\text{O}_3$ to a phase similar to Mn_3O_4 . This is anticipated because the degree of MnO_x reduction (by the carbon substrate) decreases in the direction away from the carbon substrate surface, which was exposed to air. The annealing condition created a gradient in oxidation state of Mn ion along the thickness direction; thinner MnO_x films deposited on carbon fiber were more reduced. However, they were still mixed-valent MnO_x and there is more Mn_3O_4 phase in a thinner film (Supporting Information Figure S8–S10). It is noted that all electrodes deposited for 2, 5, 15, and 30 min have the same surface phases; the graded oxidation state remained largely the same.

Gas adsorption/desorption analysis implied that the microstructure of MnO_x underwent a dramatic rearrangement during the annealing process, producing porous, nanostructured MnO_x (Supporting Information Figure S11). The specific surface area increased from 5.21 m^2/g for amorphous MnO_2 to 261.8 m^2/g for the multivalent MnO_x , as the pore volume increased from 0.021 to 0.149 cm^3/g ($\sim 42\%$ porosity) at the same time. The formation of tunneled structure of K-incorporated MnO_2 on the surface may partially account for enlarged surface area and pore volume.^{18,28} The porous, nanostructured multivalent MnO_x is ideally suited for fast mass and charge transfer associated with energy storage processes.

To evaluate the characteristic behavior of the mixed-valent MnO_x electrodes for electrical energy storage, we performed several electrochemical measurements in a 1 M Na_2SO_4

solution. The mixed-valent MnO_x electrode showed excellent “square-shape” cyclic voltammograms at 50 mV/s (Figure 3a) with current densities being almost 1 order of magnitude higher than those of the amorphous MnO_2 electrode. The symmetric shape and the instant response upon the reversal of voltage indicate that surface reactions are highly reversible and very fast. It is noted that the contribution of the porous carbon fiber substrate to the capacitance is negligible.

We have also measured the internal resistance of the electrochemical capacitors when the potentials were reversed (Supporting Information Figure S12) and plotted them as a function of applied current densities (Figure 3b). The slopes of the plots correspond directly to the equivalent series resistances (ESR) of the capacitors. This internal resistance critically influences the power density (or rate capability) of electrochemical capacitors; low capacitance and deviation from ideal capacitor behavior are usually associated with large ESR. It is clearly shown that the mixed-valent MnO_x displayed much smaller ESR than the amorphous MnO_2 at a given current density due most likely to enhanced rates of the surface redox reactions. This observation was further confirmed by the impedance measurements (insert of Figure 3b). The charge-transfer resistance (the diameter of the semicircle in the impedance spectrum) of the mixed-valent MnO_x was much smaller than that of the amorphous MnO_2 . The long tail at low frequencies of the mixed-valent MnO_x is closer to a vertical line for an ideal capacitor, another indication that the mixed-valent MnO_x has higher capacitance and lower resistance than the amorphous MnO_2 .

Typical charge–discharge curves at a constant current of 0.61 A/g are shown in Figure 3c. The “linear” and symmetrical charge–discharge curves indicate again high Coulombic efficiency or excellent reversibility. The specific capacitance (calculated from the discharge curve) of the amorphous MnO_2 was 333 F/g, comparable to the values reported in the literatures.^{26,29} In contrast, the specific capacitance for the mixed-valent MnO_x (of ~ 70 nm thick) was ~ 2530 F/g, almost eight times higher than that of the amorphous MnO_2 (of the same loading). This represents the highest specific capacitance ever reported among all known pseudocapacitor materials, including MnO_2 (1145 F/g; film <40 nm thick in a 100 nm porous Au film),¹⁷ $\text{Ni}(\text{OH})_2$ (1335 F/g; nanoplates <10 nm thick),³⁰ and RuO_2 (1340 F/g; nanodots with 2–3 nm in diameter)³¹ when all normalized to the weight of the active material only.

Because high rate capability is the most important feature of electrochemical capacitors, we measured the performance at very high cycling rates. Typically, the capacitance of a pseudocapacitor may decrease with operating current density due to mass transport limitations, especially when insertion (or removal) of ions into (or from) the electrode subsurface is involved. Much to our surprise, however, the capacitance of the mixed-valent MnO_x was not kinetically limited even at very high cycling rates (Supporting Information Figure S13), demonstrating ~ 2430 F/g at 122.7 A/g. Further, the mixed-valent MnO_x electrode displayed remarkable long-term cycling stability; cyclic voltammograms collected after 100 000 and 200 000 cycles (Figure 3d) showed little change, whereas the capacitance of the amorphous MnO_2 was much lower and degraded considerably during cycling (Supporting Information Figure S14–15). It was also found that symmetric pseudocapacitors constructed from the mixed-valent MnO_x showed very

stable performance up to 1.0 V (Supporting Information Figure S16).

It is noted, however, that the specific capacitance drops with the thickness of the MnO_x film (or loading), suggesting that only a thin film was fully utilized (or the nanoporous surface phases make dominating contributions to the observed capacitance) (Supporting Information Figure S17–18). This is not surprising because the charge storage in a capacitor is primarily confined to the surface and subsurface (or a thin layer). To increase the performance of electrochemical capacitors by increasing the film thickness of active materials is proven ineffective and, perhaps, fundamentally unattainable; after all, the rate capability may ultimately diminish with film thickness. However, our results demonstrate that it may be unnecessary to increase film thickness because the charge storage capacity of the MnO_x film can be dramatically enhanced (~ 8 times) by creating mixed-valent nanostructure, achieving values much higher than the “theoretical capacity” previously believed (e.g., ~ 1370 F/g for MnO_2 under similar conditions).⁸ Indeed, the estimated specific energy density of the ~ 70 nm thick mixed-valent MnO_x film (single electrode in a voltage window between 0 and 1.0 V) reached ~ 352 Wh/kg at a power density of ~ 614 W/kg and showed little dependence on cycling rate, still retaining ~ 337 Wh/kg at power densities up to ~ 117 800 W/kg (full charge or discharge in 10 s) when all normalized to the weight of active material only. The demonstrated specific energy densities of single electrode are much higher than those of the state-of-art pseudocapacitor materials^{27,30} (Note the voltage window for MnO_2 and $\text{Ni}(\text{OH})_2$ were 0.8 and 0.55 V in two- and three-electrode configuration, respectively) and even comparable to those of high-performance battery materials such as FePO_4 nanowires (~ 300 Wh/kg at ~ 4000 W/kg) and $\text{Li}(\text{Ni}_{0.5}\text{Mn}_{0.5})\text{O}_2$ (~ 600 Wh/kg at ~ 6000 W/kg) while retaining much higher gravimetric power (when all normalized to the weight of the electrode material only).^{32,33} Although significantly improved performance has been achieved in this study with a nanoscale coating, the mixed-valent MnO_x shows great potential to provide an order of magnitude increase in practical energy density of electrochemical capacitors without penalizing power density. We believe that MnO_x coatings must be thin to offer the best possible power density. Therefore, one effective approach to increasing practical energy density (e.g., loading) without compromising the specific capacitance or rate capability is to use nanocarbon fibers, thus increasing the surface area of CFP for conformal coating of MnO_x .

The phase composition and nanostructure of the electrode material is very sensitive to the annealing conditions. For example, when the annealing temperature was increased from 400 to 450 °C (but still in air for 2 h), XRD analysis suggested that the Mn_3O_4 phase was converted to $\alpha\text{-Mn}_2\text{O}_3$ (Supporting Information Figure S19). Similarly, when the annealing atmosphere was changed from air to N_2 and 4% H_2 balanced with Ar (still at 400 °C for 2 h), the as-synthesized amorphous MnO_2 on CFP was converted to pure Mn_3O_4 and a mixture of MnO and Mn_3O_4 , respectively (Supporting Information Figure S20). Further, the amorphous MnO_2 powder sample (synthesized under the same conditions but without carbon support) remained amorphous when annealed at 400 °C, but transformed to crystalline $\alpha\text{-Mn}_2\text{O}_3$ when annealed at 500 °C, in air for 2 h in the absence of carbon (Supporting Information Figure S21). Electrodes made of these phases performed poorly, far inferior to that of the electrodes made of the

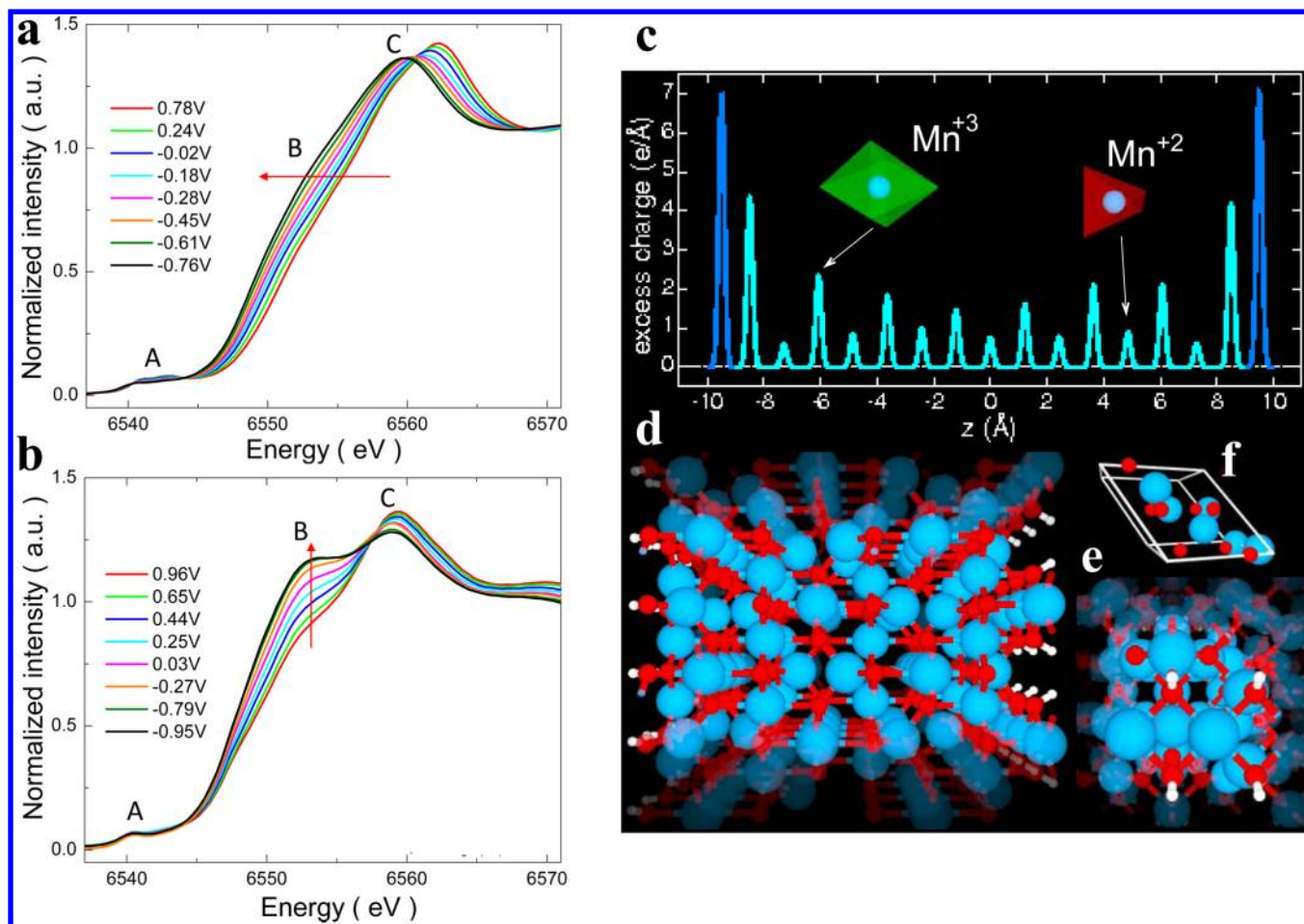


Figure 4. Investigation into the charge storage mechanism. (a) In situ XANES spectra of the as-synthesized (amorphous MnO₂) and (b) the mixed-valent MnO_x electrode during discharge in 1.0 M Na₂SO₄ electrolyte. A, B, and C represent pre-edge ($1s \rightarrow 3d$ transition), covalent character between Mn(3d) and O(2p) bond due to LMCT, and main edges ($1s \rightarrow 4p$ transition). (c) Linear excess charge distribution across the slab of Mn₃O₄ as derived from PBE+U calculations. The distribution is normalized to the number of excess electrons added to the slab model. The charge accumulated at the surface is shown in blue, while the cyan color is used to show the charge distribution in the bulk stored in the [MnO₄] tetrahedra and [MnO₆] octahedra, respectively. (d) Side view and (e) top view of the slab used in the PBE+U calculations. (f) Primitive unit cell of Mn₃O₄. Mn and O atoms are shown in blue and red colors, respectively.

multivalent MnO_x created by annealing in air at 400 °C for 2 h (Supporting Information Figure S19–S20).

Since the mixed-valent phases seem to play a pivotal role in achieving the anomalously high capacitance, we performed both ex situ and in situ XAS to gain some insights into the charge-storage mechanism of the mixed-valent MnO_x electrodes (Supporting Information Figure S22–S23). The in situ X-ray absorption near edge spectroscopy (XANES) spectra (Figure 4a) for the as-synthesized MnO₂ electrodes acquired during the first discharge (0.8 to –0.8 V) showed an entire edge shift toward lower energy in a continuous manner, suggesting that the charge storage is mostly associated with the Mn³⁺/Mn⁴⁺ redox reactions, as conventionally believed. In contrast, however, the XANES spectra (Figure 4b) for the mixed-valent MnO_x collected under the identical conditions (except over a wider voltage window from 1.0 to –1.0 V) showed completely different spectral features that have never before been reported. First, there was no obvious entire edge shift during discharge, although a slight edge shift toward lower energy was observed, indicating a decrease in average oxidation state of Mn ions. The average change in Mn valence (calculated from the edge shift) for both cases was similar: ~0.3 within a voltage window of 0.0

to 0.8 V (Supporting Information Figure S23); yet, the observed specific capacitance for the mixed-valent MnO_x is much higher (~8 times) than that for the as-prepared MnO₂ sample. Clearly, the change in oxidation state of Mn ion cannot account for the anomalous pseudocapacitive behavior. Second, the dominating spectral feature is a unique evolution of the shoulder peak (B), which is related to the ligand-to-metal charge transfer (LMCT) process. The increased B peak intensity indicates the increased degree of covalent character of Mn(3d)-O(2p) bonding during the discharge. Thus, the unique Mn K-edge change in the form of increasing B feature clearly shows that a large portion of the charge compensation might be originated from the hole state redistribution toward the oxygen sites, rather than just the reduction of Mn ion (as seen for the as-synthesized MnO₂), suggesting that the unique atomic and electronic structure (Supporting Information Figure S22) of the nanostructured, mixed-valent MnO_x may allow additional charge compensation mechanism, which has not been observed in MnO₂. Although small intensity change of B feature in XANES spectra during charge–discharge were reported in the literature^{34,35} for transition metal K-edges such as Co and Mn, it has never before been observed that

these spectral changes (LMCT) play a dominating role over the continuous edge shift (redox reaction of cations).

The role of oxygen anions for charge compensation in transition metal oxides is not unprecedented; it was previously argued for lithium battery electrodes. Aydinol et al. showed that more charge can be transferred to the oxygen anions than to the metal cations in the oxide upon intercalation of lithium ions.³⁶ To estimate the charge distribution in the nanoporous multivalent MnO_x (with dominant phase of Mn_3O_4), we resorted to spin-polarized density functional theory (DFT) calculations. To model the geometry of Mn_3O_4 nanoneedles (as seen in Figure 1g), we used a tetragonal slab of Mn_3O_4 exposing to the vacuum two opposite (001) surfaces of area $5.94 \times 5.94 \text{ \AA}^2$ and having a linear dimension perpendicular to the surface of 19.5 \AA . Our DFT calculations (Figure 4c) show that significant amount of the excess negative charge is indeed accumulated at the surface of the Mn_3O_4 nanoneedles. In the bulk, the excess negative charge gradually decays from the surface peak, localizing prevalently in correspondence of the Mn^{3+} ions in the $[\text{MnO}_6]$ octahedra rather than at the Mn^{2+} centers in the $[\text{MnO}_4]$ tetrahedra. An analysis of the individual Bader atomic charges³⁷ shows, in particular, that the percentage of excess charge stored at the surface and in the bulk of Mn_3O_4 is 36 and 64%, respectively, while in the bulk the negative charge accumulated at or in proximity of Mn^{2+} , Mn^{3+} , and O centers is 15, 50, and 35%, respectively.

Our DFT calculations therefore suggest that the amounts of excess charge accumulated on the surface and at O centers are significant, consistent with our in situ XAS results. Charge accumulation on O centers appear to be favored by the close proximity of the Mn^{3+} species that, thanks to the good hybridization of the Mn^{3+} 3d and the O 2p orbitals, spill the excess negative charge onto the neighboring O atoms. These new charge compensation mechanisms at O centers and surfaces directly challenge the traditional notion that pseudocapacitance is primarily associated with redox reaction of cations.

Additionally, the coexistence of aliovalent cations (Mn^{2+} , Mn^{3+} , and Mn^{4+}) may facilitate the formation of more ionic defects (e.g., vacancies and misplaced ions) and electronic defects (electrons and holes), thus altering the electronic, ionic, and catalytic properties of the manganese oxides. These defects may accelerate the kinetics of the surface redox reactions. Also, the mismatches induced by structural differences among different manganese oxide phases may produce additional defects (cavities, stacking faults, etc.), thus facilitating the formation of porous nanoarchitectures that may enhance the transport of charged species and extend the reaction sites from the surface to the subsurface of electrode. Recent theoretical studies predicted that photoconductivity of MnO_2 can be enhanced by introducing Ruetschi defects or protonated Mn(IV) vacancies, suggesting that electronic properties can be tailored by tuning the defect structure during synthesis.³⁸

Our results suggest that electrochemical capacitors based on this MnO_x film have potential to reach energy densities much higher than those of existing pseudocapacitors while maintaining high rate capabilities and excellent cycling performance of EDLCs. This can be accomplished by the creation of thin films of mixed-valent manganese oxides with porous nanoarchitecture, enabling multiple charge storage mechanisms with much smaller internal resistance and highly reversible, faster charge transfer kinetics. Although we have focused on MnO_x as active materials for pseudocapacitors in this study, other transition

metal oxides could also be explored using a similar method to design mixed-valent nanostructures/carbon composites with significantly enhanced electrochemical performances for other applications.

■ ASSOCIATED CONTENT

📄 Supporting Information

Additional figures and experimental details are included. This material is available free of charge via the Internet at <http://pubs.acs.org>.

■ AUTHOR INFORMATION

Corresponding Author

*E-mail: meilin.liu@mse.gatech.edu.

Author Contributions

#These authors contributed equally to this work.

Notes

The authors declare no competing financial interest.

■ ACKNOWLEDGMENTS

This material is based upon work supported as part of the HeteroFoam Center, an Energy Frontier Research Center funded by the U.S. Department of Energy (DOE), Office of Science, Office of Basic Energy Sciences (BES) under Award Number DE-SC0001061. The authors acknowledge the use of the X14A beamline at Brookhaven National Laboratory (BNL, partially sponsored by the U.S.-DOE-EERE, Vehicle Technologies Program, through the HTML User Program at ORNL) and the SHaRE User Facility at Oak Ridge National Laboratory (ORNL, sponsored by the Scientific User Facilities Division, US-DOE-BES). K.W.N. and X.Q.Y. are supported by the U.S.-DOE Assistant Secretary for EERE, Office of Vehicle Technologies, Vehicle Technology Program, under Contract Number DEAC02-98CH10886. Partial support of the WCU program at UNIST is also acknowledged. M.K.S. and S.C. thank K. Blinn, S. Lai, and M. F. Liu for their help on Raman spectroscopy and TGA measurements.

■ REFERENCES

- (1) Whittingham, M. S. *MRS Bull.* **2008**, 33 (4), 411–419.
- (2) Conway, B. E. *Electrochemical Supercapacitors*; Kluwer-Academic: New York, 1999.
- (3) Chmiola, J.; Yushin, G.; Gogotsi, Y.; Portet, C.; Simon, P.; Taberna, P. L. *Science* **2006**, 313 (5794), 1760–1763.
- (4) Simon, P.; Gogotsi, Y. *Nat. Mater.* **2008**, 7 (11), 845–854.
- (5) Hall, P. J.; Mirzaei, M.; Fletcher, S. I.; Sillars, F. B.; Rennie, A. J. R.; Shitta-Bey, G. O.; Wilson, G.; Cruden, A.; Carter, R. *Energy Environ. Sci.* **2010**, 3 (9), 1238–1251.
- (6) Brezesinski, T.; Wang, J.; Tolbert, S. H.; Dunn, B. *Nat. Mater.* **2010**, 9 (2), 146–151.
- (7) Lee, H. Y.; Goodenough, J. B. *J. Solid State Chem.* **1999**, 144 (1), 220–223.
- (8) Toupin, M.; Brousse, T.; Belanger, D. *Chem. Mater.* **2004**, 16 (16), 3184–3190.
- (9) Yu, G.; Hu, L.; Liu, N.; Wang, H.; Vosgueritchian, M.; Yang, Y.; Cui, Y.; Bao, Z. *Nano Lett.* **2011**, 11 (10), 4438–4442.
- (10) Yu, G.; Hu, L.; Vosgueritchian, M.; Wang, H.; Xie, X.; McDonough, J. R.; Cui, X.; Cui, Y.; Bao, Z. *Nano Lett.* **2011**, 11 (7), 2905–2911.
- (11) Hu, L.; Pasta, M.; Mantia, F. L.; Cui, L.; Jeong, S.; Deshazer, H. D.; Choi, J. W.; Han, S. M.; Cui, Y. *Nano Lett.* **2010**, 10 (2), 708–714.
- (12) Raymundo-Pinero, E.; Khomeiko, V.; Frackowiak, E.; Beguin, F. *J. Electrochem. Soc.* **2005**, 152 (1), A229–A235.

- (13) Chou, S. L.; Wang, J. Z.; Chew, S. Y.; Liu, H. K.; Dou, S. X. *Electrochem. Commun.* **2008**, *10* (11), 1724–1727.
- (14) Fischer, A. E.; Pettigrew, K. A.; Rolison, D. R.; Stroud, R. M.; Long, J. W. *Nano Lett.* **2007**, *7* (2), 281–286.
- (15) Lee, S. W.; Kim, J.; Chen, S.; Hammond, P. T.; Shao-Horn, Y. *ACS Nano* **2010**, *4* (7), 3889–3896.
- (16) Chen, S.; Zhu, J.; Wu, X.; Han, Q.; Wang, X. *ACS Nano* **2010**, *4* (5), 2822–2830.
- (17) Lang, X. Y.; Hirata, A.; Fujita, T.; Chen, M. W. *Nat. Nanotechnol.* **2011**, *6* (4), 232–236.
- (18) Post, J. E. *Proc. Natl. Acad. Sci. U.S.A.* **1999**, *96* (7), 3447–3454.
- (19) Shen, Y. F.; Zenger, R. P.; Deguzman, R. N.; Suib, S. L.; McCurdy, L.; Potter, D. I.; Oyoung, C. L. *Science* **1993**, *260* (5107), 511–515.
- (20) Tian, Z. R.; Tong, W.; Wang, J. Y.; Duan, N. G.; Krishnan, V. V.; Suib, S. L. *Science* **1997**, *276* (5314), 926–930.
- (21) Hankache, J.; Wenger, O. S. *Chem. Rev.* **2011**, *111* (8), 5138–5178.
- (22) Robin, M. B.; Day, P. Mixed Valence Chemistry-A Survey and Classification. In *Advances in Inorganic Chemistry*; Emeléus, H. J., Sharpe, A. G., Eds.; Academic Press: New York, 1968; Vol. 10, pp 247–422.
- (23) Young, C. G. *Coord. Chem. Rev.* **1989**, *96*, 89–251.
- (24) Varma, C. M. *Rev. Mod. Phys.* **1976**, *48* (2), 219–238.
- (25) Ragupathy, P.; Park, D. H.; Campet, G.; Vasani, H. N.; Hwang, S. J.; Choy, J. H.; Munichandraiah, N. *J. Phys. Chem. C* **2009**, *113* (15), 6303–6309.
- (26) Xu, M. W.; Zhao, D. D.; Bao, S. J.; Li, H. L. *J. Solid State Electrochem.* **2007**, *11* (8), 1101–1107.
- (27) Subramanian, V.; Zhu, H. W.; Wei, B. Q. *Electrochem. Commun.* **2006**, *8* (5), 827–832.
- (28) Gao, T.; Glerup, M.; Krumeich, F.; Nesper, R.; Fjellvag, H.; Norby, P. *J. Phys. Chem. C* **2008**, *112* (34), 13134–13140.
- (29) Hu, C. C.; Tsou, T. W. *Electrochem. Commun.* **2002**, *4* (2), 105–109.
- (30) Wang, H.; Casalongue, H. S.; Liang, Y.; Dai, H. J. *Am. Chem. Soc.* **2010**, *132* (21), 7472–7477.
- (31) Hu, C. C.; Chen, W. C.; Chang, K. H. *J. Electrochem. Soc.* **2004**, *151* (2), A281–A290.
- (32) Lee, Y. J.; Yi, H.; Kim, W. J.; Kang, K.; Yun, D. S.; Strano, M. S.; Ceder, G.; Belcher, A. M. *Science* **2009**, *324* (5930), 1051–1055.
- (33) Kang, K. S.; Meng, Y. S.; Breger, J.; Grey, C. P.; Ceder, G. *Science* **2006**, *311* (5763), 977–980.
- (34) Yoon, W. S.; Balasubramanian, M.; Chung, K. Y.; Yang, X. Q.; McBreen, J.; Grey, C. P.; Fischer, D. A. *J. Am. Chem. Soc.* **2005**, *127* (49), 17479–17487.
- (35) Kim, M. G.; Shin, H. J.; Kim, J. H.; Park, S. H.; Sun, Y. K. *J. Electrochem. Soc.* **2005**, *152* (7), A1320–A1328.
- (36) Aydinol, M. K.; Kohan, A. F.; Ceder, G.; Cho, K.; Joannopoulos, J. *Phys. Rev. B* **1997**, *56* (3), 1354–1365.
- (37) Bader, R. F. W. *Atoms in Molecules - A Quantum Theory*; Oxford University Press: New York, 1990.
- (38) Kwon, K. D.; Refson, K.; Sposito, G. *Phys. Rev. Lett.* **2008**, *100*, 146601.

Supplementary Information

**Anomalous Pseudocapacitive Behavior of a Nanostructured,
Mixed-Valent Manganese Oxide Film for Electrical Energy Storage**

Min-Kyu Song^{1,†}, Shuang Cheng^{1,†}, Haiyan Chen², Wentao Qin¹, Kyung-Wan Nam³, Shucheng Xu⁴, Xiao-Qing Yang³, Angelo Bongiorno⁴, Jangsoo Lee⁵, Jianming Bai⁶, Trevor A. Tyson², Jaephil Cho⁵, and Meilin Liu^{1,*}

¹*School of Materials Science and Engineering, Center for Innovative Fuel Cell and Battery Technologies, Georgia Institute of Technology, 771 Ferst Drive, Atlanta, GA 30332-0245, USA*

²*Department of Physics, New Jersey Institute of Technology, Newark, NJ 07102, USA*

³*Chemistry Department, Brookhaven National Laboratory, Upton, NY 11973, USA*

⁴*School of Chemistry and Biochemistry, Georgia Institute of Technology, 901 Atlantic Drive, Atlanta, GA 30332-0400, USA*

⁵*Interdisciplinary School of Green Energy, Ulsan National Institute of Science & Technology (UNIST), 701-11,100 Banyeon-ri, Eonyang-eup, Ulju-gun, Ulsan, Korea, 689-798*

⁶*High Temperature Materials Laboratory, Oak Ridge National Laboratory, Oak Ridge, TN 37831, USA*

† These authors contributed equally to this work.

* e-mail: meilin.liu@mse.gatech.edu

Methods

Synthesis of novel electrodes. All chemicals were of analytical grade and used without further purification. In a typical synthesis procedure, several pieces of carbon fiber paper (Fuel cell store, 2050L) were added into 100 ml of 2M sulfuric acid (H_2SO_4 solution), pre-heated to a given temperature (75°C) in a water bath with vigorous magnetic stirring with cool water fluxing in about 30 min. One gram of KMnO_4 was subsequently added to the solution which was kept for a predetermined period of time (2~30 minutes) with vigorous stirring. The morphology and nanostructure of MnO_x coating can be tuned by adjusting the solution temperature ($60\sim 90^\circ\text{C}$). The as-synthesized electrodes were then taken out, ultrasonically cleaned for several times with DI water and ethanol, dried at 80°C for about an hour, and annealed for 2 hours at different temperatures (200, 350, 400, 450°C) in different atmospheres (air, N_2 , 4% H_2) with a ramp rate of $3^\circ\text{C}/\text{min}$. It is noted that different types of carbon (e.g., carbon nanotubes and graphene) or different diameter of carbon fibers would require slightly different annealing conditions to form the mixed-valent MnO_x film.

Electron microscopy. Scanning electron microscope (SEM Leo/Zeiss 1530) was operated at an accelerating voltage of 3 kV and the high resolution transmission electron microscope (JEOL 4000 EX) was operated at an accelerating voltage of 400kV.

Synchrotron-based X-ray analysis (Diffraction and Absorption). Synchrotron X-ray diffraction analyses, including glancing angle and time-resolved X-ray diffraction, were carried out with the beamline X14A of the National Synchrotron Light Source (NSLS) at Brookhaven National Laboratory. Diffraction patterns were collected with a high resolution Si strip detector of 640 pixels, with each pixel corresponding to 0.005° . For *in-situ* XRD studies, each as-synthesized sample was loaded into a quartz capillary (inner diameter 0.7 mm) of a flow cell and air was admitted into the cell at a rate of 10 mL/min. The resistive heating of the capillary was program-controlled by a temperature controller (Eurotherm 818) and monitored with a 0.5-mm type K thermocouple inside the capillary. Phase identifications were performed using software Jade 6.5 (Materials Data INC). The *ex situ* X-ray absorption (XANES and XAFS) data were collected at NSLS beamline

X3B. The measurements were collected in fluorescence mode using a 13-element Ge detector. A Mn metal powder sample was used for energy calibration. *In situ* Mn K-edge XAS during charge-discharge of the cell was measured at the beamlines X18A and X19A in a fluorescence mode using a PIPS detector. The reference Mn foil spectra were also measured simultaneously in a transmission mode for an energy calibration.

Electrochemical characterization. Cyclic voltammetry (CV) curves and galvanostatic charge-discharge curves were recorded at room temperature in a symmetric-cell configuration containing 1M Na₂SO₄ electrolyte solution. The Whatman filters (GF/D) were used as separators and typical area of single electrode was ~1.98cm². It is noted that, due to the macro-porous feature of CFP and thin, conformal coating of MnO_x film, scale-up can be easily made by stacking the electrodes up to several layers without compromising excellent performance (Fig. S17). The potential and current were controlled by an Electrochemical Interface (Solartron, SI 1286) and the electrochemical impedance spectroscopy (EIS) analysis was conducted using a Frequency Response Analyzer (Solartron SI 1255) and SI 1286 with an applied ac voltage of 10 mV in the frequency range of 0.001 Hz to 1 MHz.

The symmetrical cell of “two identical electrodes” was used for estimation of specific capacitances, energy density and power density, except when we examined the electrochemical behavior of the active electrode materials using three-electrode configurations (e.g., with respect to a reference electrode, Figure S16). When a symmetric cell of “two identical electrodes” is used, the apparent capacitance of the cell, C_{total}, is related to the capacitances of two electrodes as follows,

$$\frac{1}{C_{total}} = \frac{1}{C_{+}} + \frac{1}{C_{-}} \quad (1)$$

where C₊ and C₋ are the capacitance of each single electrode in the symmetrical cell. When the two electrodes are “identical” (i.e., C₊ ≈ C₋), the capacitance of each single electrode can be calculated from the capacitance of the cell as follows,

$$C_{+} \approx C_{-} \approx 2C_{Total}$$

The capacitance was calculated from the slope of the discharge curve from the following equation:

$$C_{Total} = \frac{I}{\left(\frac{dV}{dt}\right)} \quad (2)$$

where C_{Total} is the capacitance of the symmetric cell in Farad (F), I is the discharge current in Ampere (A) and dV/dt is the slope of the discharge curve in Volts per second (V/s). Thus, the specific capacitance of active material (F/g) per single electrode is related to the capacitance of the symmetric cell, C_{Total} , as follows,

$$C_{m,AM} = \frac{2C_{Total}}{m_{AM}} \quad (3)$$

where m_{AM} is the weight (g) of the active material (MnO_x) per single electrode.

The maximum stored energy (E) and the peak power (P) of electrochemical capacitors are given by equations (4) and (5), respectively, where C is the capacitance in Farads, V is the operating voltage in volts, and R is the equivalent series resistance in ohms.

$$E = \frac{1}{2} CV^2 \quad (4)$$

$$P = \frac{V^2}{4R} \quad (5)$$

The power density was calculated by dividing the energy density by the discharge time (h) at different current densities. The calculated energy and power densities were then normalized by the weight of active materials (0.32 mg, MnO_x) of single electrode. Further information about these calculations can be found elsewhere^{1,2}.

Other characterization. The thermogravimetric analysis (TGA) was used to determine the weight of the MnO_x loaded to CFP with a heating rate of 25°C/min. Typical weight of MnO_x in single electrode ranged from ~0.32 mg to ~2.8 mg depending on the deposition time (2~30 minutes). The thicknesses of the MnO_x coatings were determined from microscopy. Gas adsorption analysis (BELSORP-max, BEL JAPAN, INC) was

performed to evaluate the specific surface area (Brunauer-Emmett-Teller, BET), specific pore volumes, average pore size and nitrogen adsorption/desorption isotherm.

Computational methods. DFT calculations were performed using the Vienna Ab-initio Simulation Package (VASP)^{3,4}. An energy cutoff of 400 eV was used for the plane wave basis set, ionic cores were treated by using the projector augmented wave method^{3,4}, and the exchange and correlation energy was accounted for within the generalized gradient approximation proposed by Perdew, Burke, and Ernzerhof (PBE)⁵. To describe appropriately the manganese oxides, we employed a PBE+U scheme following the approach of Dudarev⁶ with a value for $U - J$ equal to 4 eV⁷. Surface calculations were carried out using a slab of crystalline Mn_3O_4 (Hausmannite, space group *I41/amd*), exposing (001) surfaces to a vacuum region of 12 Å. Calculations were carried out by using a 3x3x1 Monkhorst-Pack grid. To model the experimental conditions, O-atoms on the surface were terminated by H atoms. The excess charge added to the slab was 0.5e per formula unit. The charge density obtained from the VASP calculations was analyzed according to the Quantum Theory of Atoms in Molecules⁸.

Supplementary Figures and Discussion

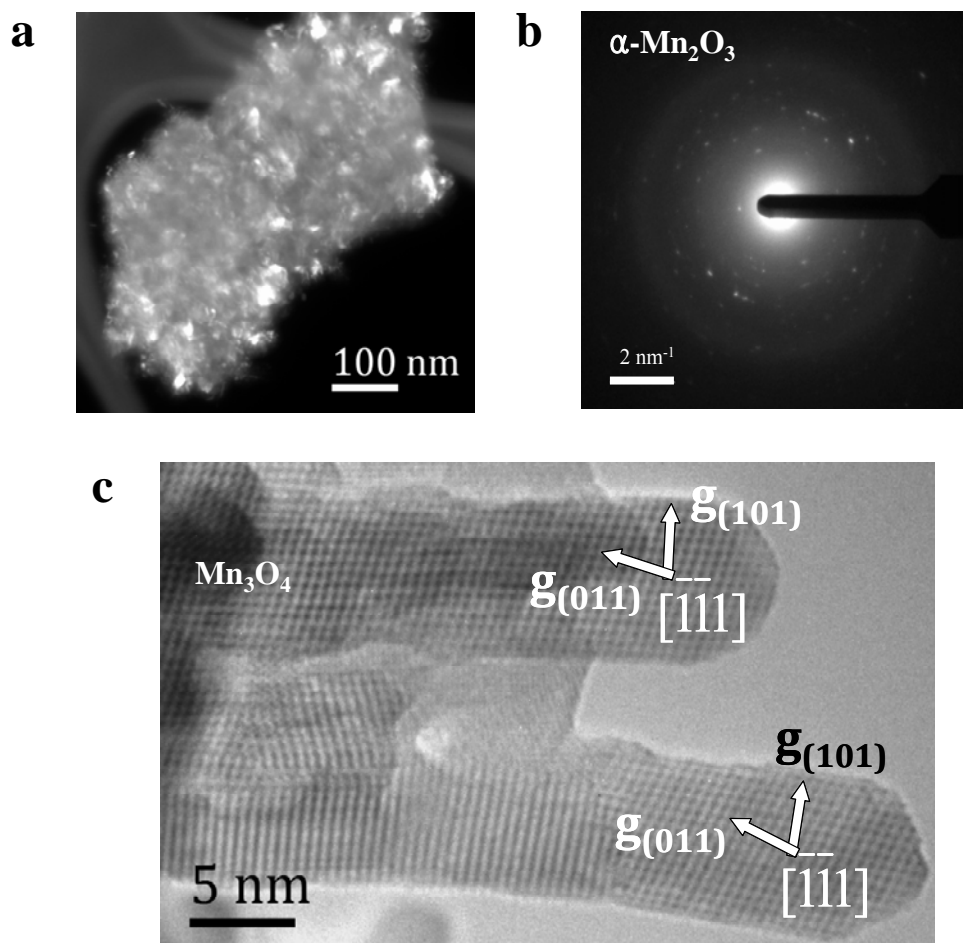


Fig. S1. **a**, A dark-field image of a portion of a crushed MnO_x coated CFP after annealing in air at 400°C for 2h. **b**, Selected area electron diffraction (SAED) pattern of the sample shown in (a). **c**, High resolution TEM image showing the $[\bar{1}\bar{1}\bar{1}]$ zone-axis fringes of two Mn_3O_4 nano-needles, whose diameters are on the order of a few nanometers.

The MnO_x coated CFP sample was rigorously pestled in a mortar to a fine powder form. The fine powders were dispersed in isopropyl alcohol, and subsequently loaded on a lacey carbon film on a Cu grid. Figure (a) reveals the low aspect-ratio particles in the size

range of tens of nanometers; in addition, there are many smaller crystals of a few nanometers lit up. The SAED pattern shown in Fig. (b) shows many discrete and conspicuous diffraction spots, all of which can be indexed with the crystalline α - Mn_2O_3 with a lattice constant of 0.94 nm. The lattice fringes shown in Fig. (c) reveal Mn_3O_4 crystals grown with strongly preferred orientation parallel to the (101) lattice planes. Since both the (101) and the (011) spacing are the largest lattice spacing in Mn_3O_4 lattice, such an orientation provides the maximum opening of the lattice to the outside of the nano-needle and may facilitate the incorporation and transport of ions along this direction.

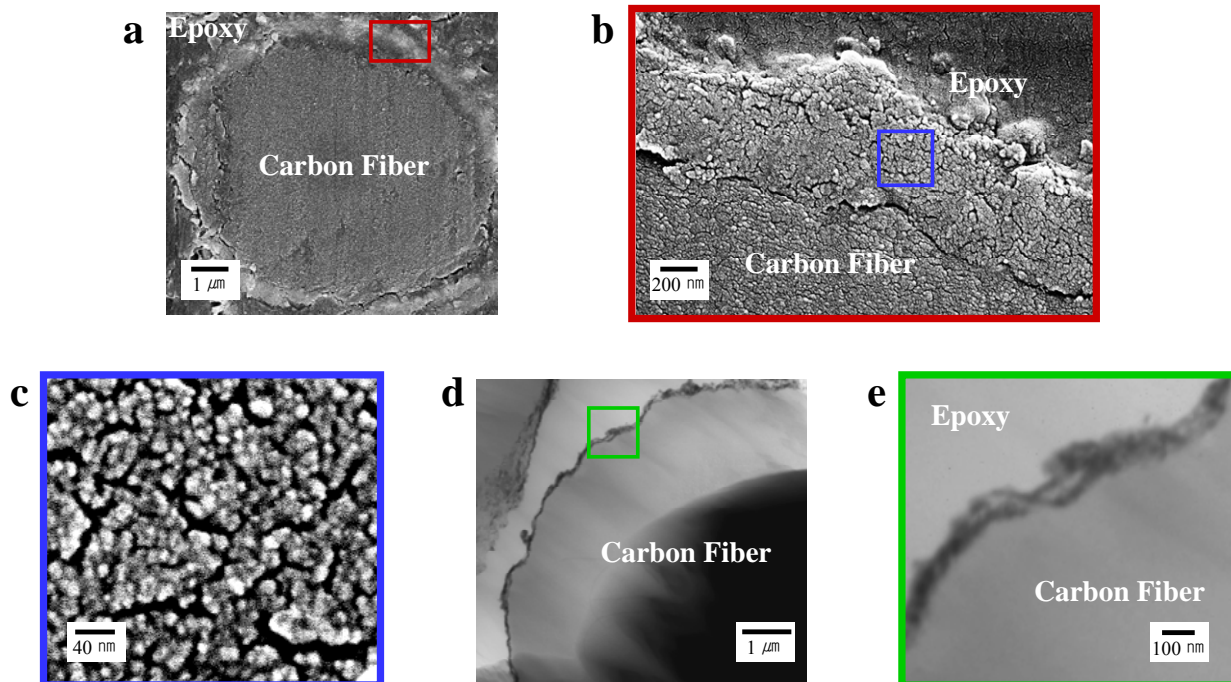


Fig. S2. **a**, Cross-sectional SEM image of MnO_x/CFP deposited for 30 minutes. **b**, An enlarged view of the area highlighted with a red rectangle in (a) showing the details of the MnO_x coating. **c**, An enlarged view of the area highlighted with a blue square in (b) showing the porous morphology of the MnO_x layer. **d**, A cross-sectional TEM image of MnO_x/CFP deposited for 2 minutes. **e**, An enlarged view of the area highlighted with a green square in (d) showing the thin MnO_x coating.

We have carefully examined the cross-sectional views of MnO_x -coated CFP with different loading of MnO_x (by deposition for a period of 2, 5, 15, and 30 minutes). Shown in Fig. S2 are some typical TEM (deposition of MnO_x for 2 min) and SEM (deposition of MnO_x for 30 min) images of MnO_x -coated CFP electrodes. The thicknesses of the MnO_x coatings can be readily seen from these images. Fig. S2 (a) shows a low-magnification cross-sectional view of a MnO_x coating deposited for 30 minutes on a carbon fiber of 8-

10 μm in diameter. The average thickness of the MnO_x coating is ~ 800 nm. Fig. S2 (c) reveals the porous structure of the MnO_x coating. For the sample prepared by deposition of MnO_x for 2 min, a very thin coating of porous MnO_x was observed along the perimeter of the carbon fibers, as seen in Figure S2 (e). The average thickness is ~ 70 nm.

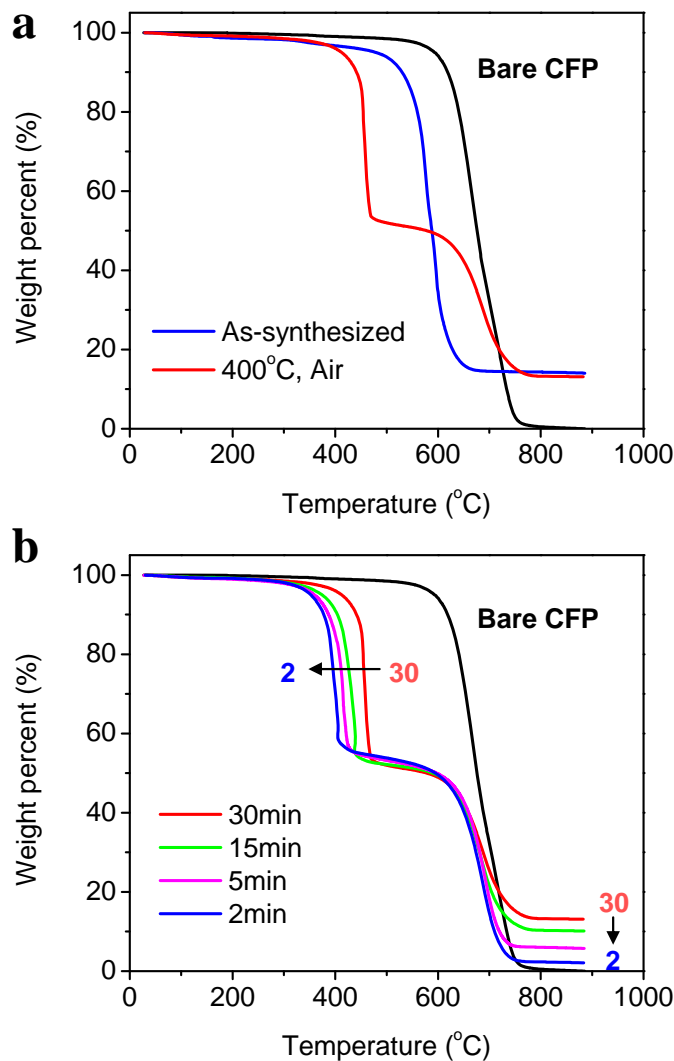


Fig. S3. a, TGA curves of bare CFP, as-synthesized MnO_2 on CFP, and mixed-valent MnO_x after heat-treatment at 400°C for 2 h. Both samples were deposited for 30 minutes. **b,** TGA curves of mixed-valent MnO_x deposited for different time (2~30 minutes).

We used thermogravimetric analysis (TGA) to determine the total weight of each MnO_x -coated CFP sample (the initial weight of the sample at room temperature after heat-treatment at 400°C for 2 h) and the weight of the MnO_x loaded to CFP (the final weight

of the sample above 800°C when all carbon were removed). We repeated the measurements many times and the standard deviation was ~ 2.8%.

As shown in Fig. S3a, while bare CFP was totally burned out above 800°C, TGA curve of as-synthesized electrode (prepared by deposition of amorphous MnO₂ for 30 minutes) indicated the weight of remaining MnO₂ is 14.3 wt.% of total electrode. The combustion (i.e. oxidation) of carbon started earlier (at ~530°C) for the as-synthesized sample than for the bare CFP (at ~630°C) due to catalytic combustion caused by manganese oxide. Interestingly, the TGA curve appears quite different for the samples annealed at 400°C in air for 2 h, which led to formation of mixed-valent MnO_x on the CFP. The catalytic combustion of carbon started even earlier (at ~430°C) than the amorphous MnO₂ and showed a two-step oxidation process. The first dramatic weight loss is attributed to the oxidation of thin carbon layer in the proximity to the MnO_x coating.

The TGA curves of MnO_x/CFP electrode deposited for 2, 5, 15 and 30 minutes are shown in Fig. S3b. Our best performance (~2,530 F/g) was achieved with the MnO_x/CFP electrode prepared by deposition of MnO_x for 2 min. The weight % of MnO_x deposited for 2, 5, 15, and 30 minutes were determined to be ~2.3%, ~4.8%, ~10.3% and ~13.3%, respectively. The thicknesses of the MnO_x coatings (determined from microscopy), together with the corresponding weights of MnO_x (determined from TGA), are plotted as a function of the deposition time in Fig. S4.

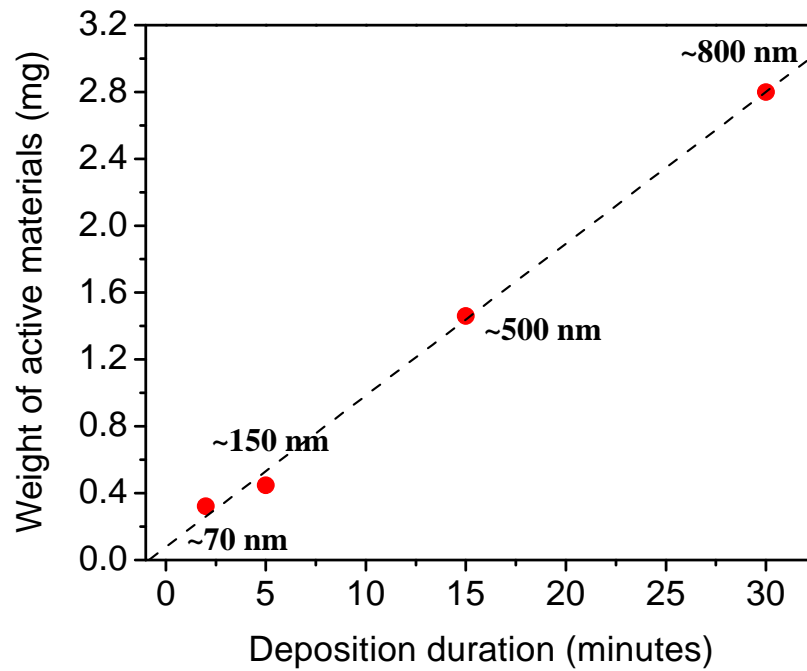


Fig. S4. The thickness and the weight of the MnO_x coating of single electrode with a superficial area of $\sim 1.98 \text{ cm}^2$. The weights of MnO_x were determined using TGA whereas the thickness was determined by electron microscopy.

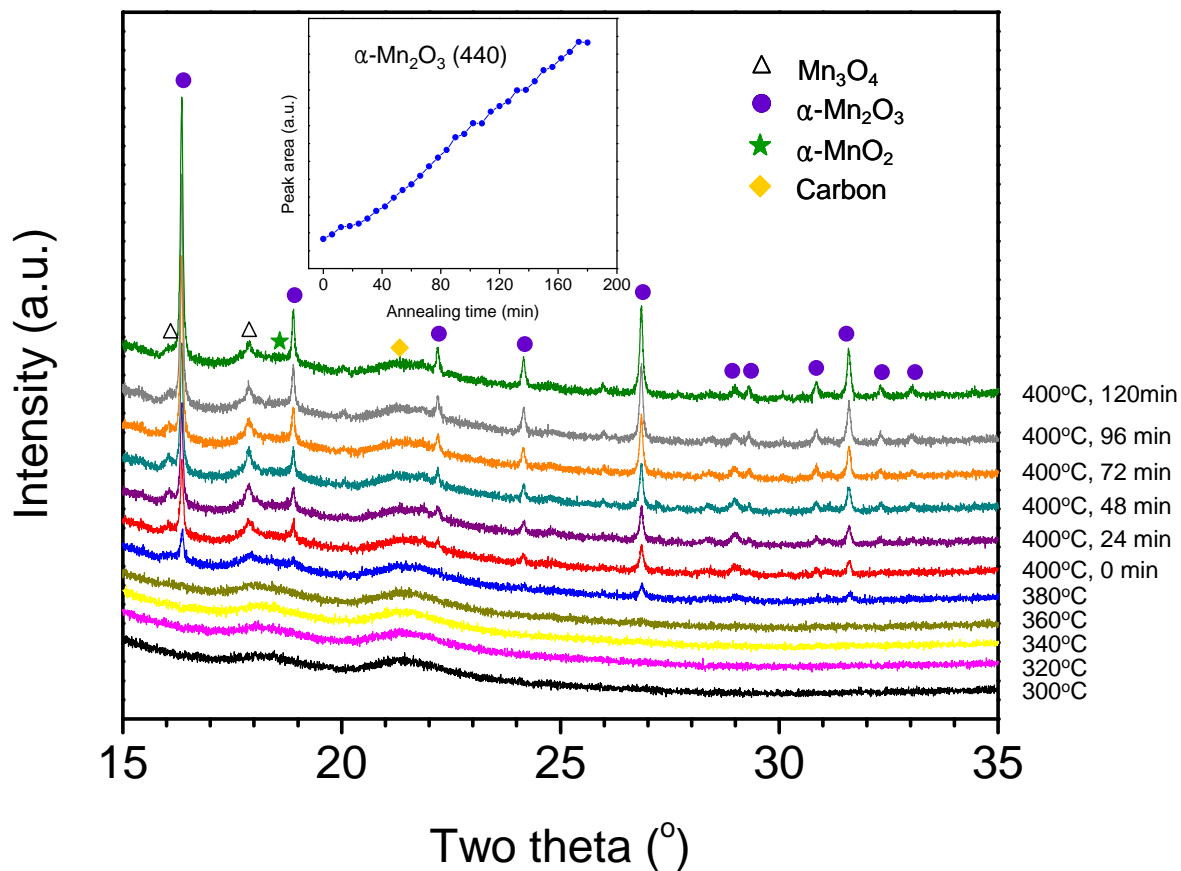


Fig. S5. *In-situ* synchrotron-based XRD patterns (transmission mode) of MnO_x coating measured at different temperatures and annealing times. The patterns reveal that small crystalline phases started to form above 360°C. At 400°C, sharp peaks of crystalline α-Mn₂O₃ appeared with small amounts of Mn₃O₄ and α-MnO₂. The α-Mn₂O₃ peak intensities grow with annealing time as shown in the insert, indicating that the volume fraction of the phase increased with annealing time. In contrast, the intensities of the Mn₃O₄ peaks decreased slightly with annealing time at 400°C. The Mn₃O₄ phase disappeared after annealing at 400°C in air for 3 hours (the result is not shown).

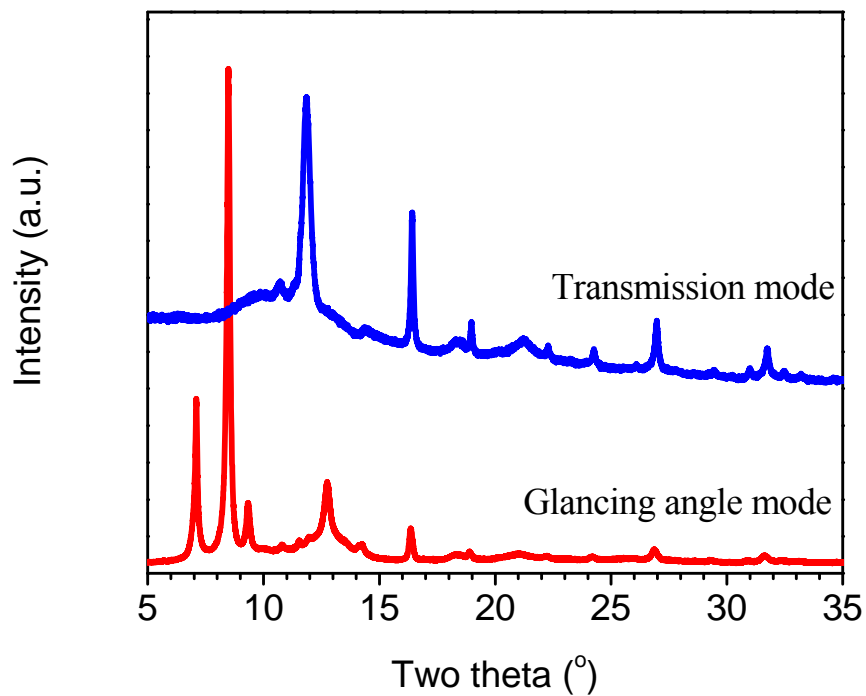


Fig. S6. Synchrotron-XRD patterns of MnO_x deposited for 30 minutes and annealed at 400°C in air for 2h. The differences between the patterns acquired in a transmission mode and a glancing angle (0.1°) mode suggest that the phases on the surface are very different from those in the bulk.

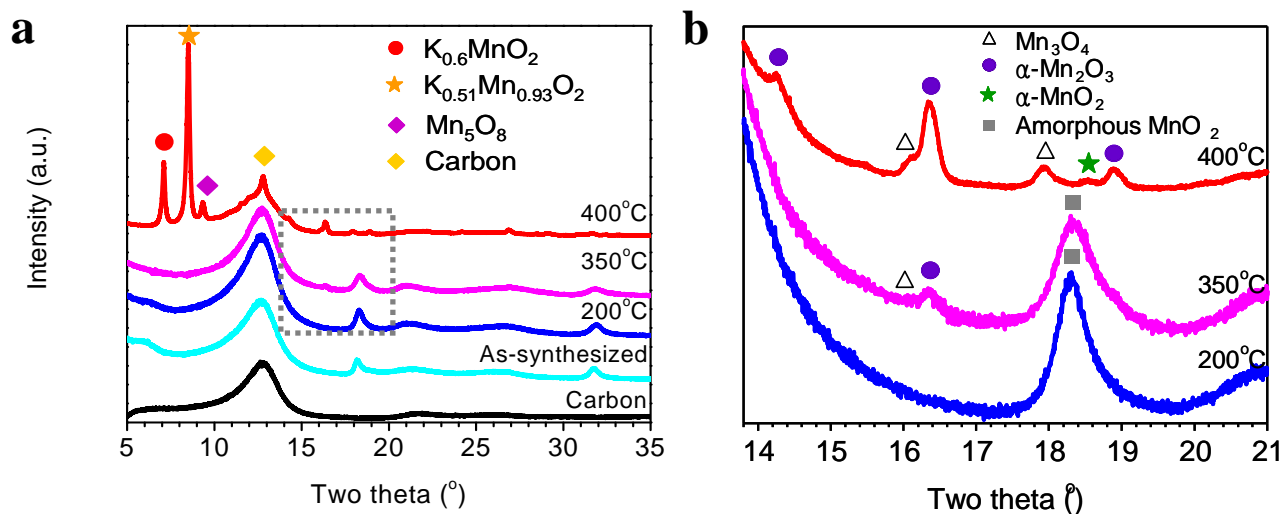


Fig. S7. a, Synchrotron-XRD patterns acquired at an incident glancing angle of 0.2° for different samples of carbon, as-coated electrode, and coated electrode annealed at different temperatures in air for 2h. It appears that the surface phases (K-incorporated MnO_2 , Mn_5O_8 , and Mn_3O_4 ,) were formed at $\sim 400^\circ\text{C}$. **b**, Enlarged view of the XRD pattern in the range of $14\sim 21^\circ$ as highlighted in (a), confirming that crystalline $\alpha\text{-Mn}_2\text{O}_3$ appeared at $\sim 400^\circ\text{C}$ with small amounts of Mn_3O_4 and $\alpha\text{-MnO}_2$. Also, it is noted that small $\alpha\text{-Mn}_2\text{O}_3$ peaks started to appear at 350°C .

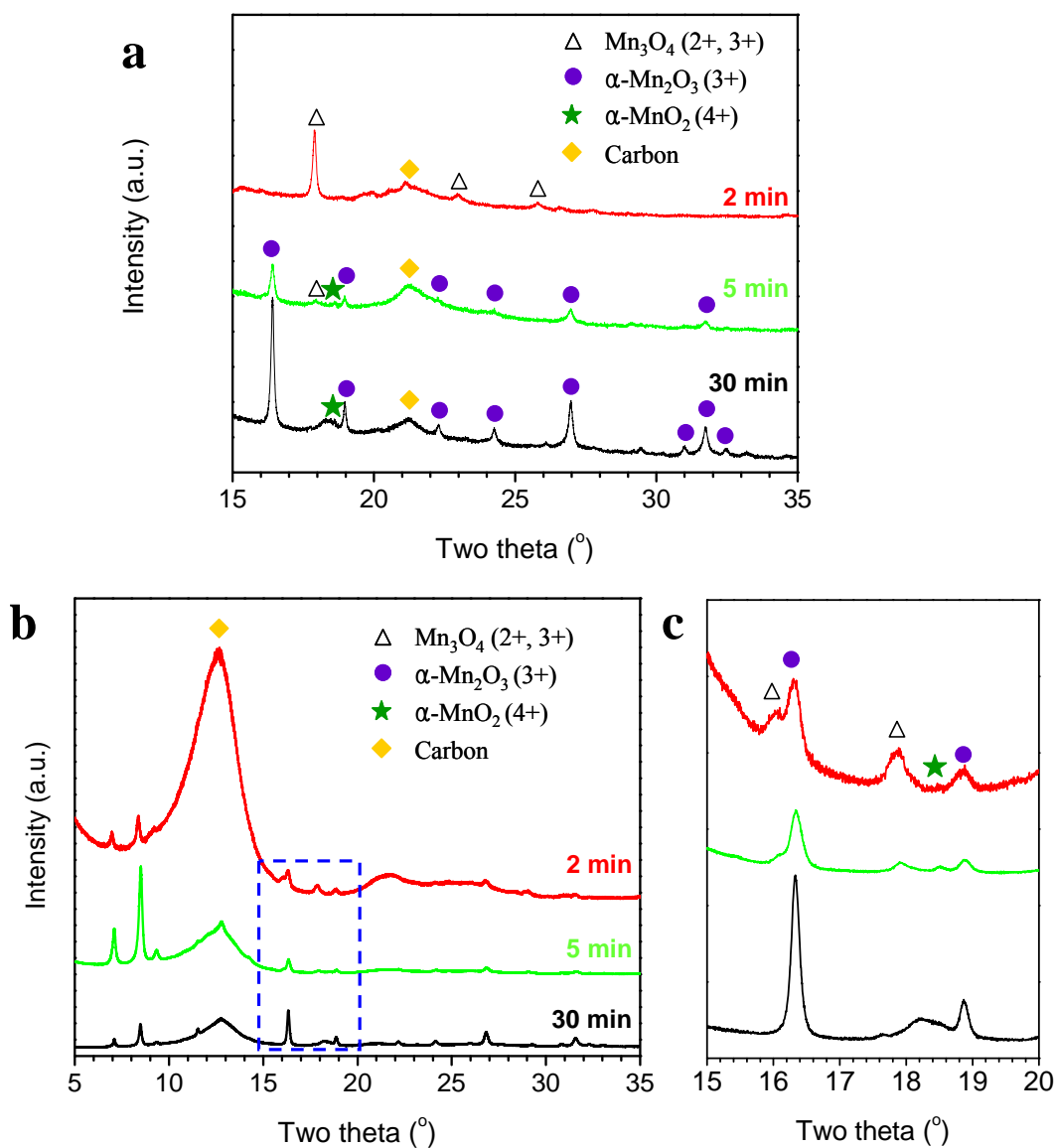


Fig. S8. Synchrotron X-ray diffraction (XRD) analysis. **a**, Transmission mode XRD pattern of MnO_x electrodes deposited for 2, 5, and 30 minutes followed by annealing at 400°C in air for 2h. **b**, Glancing angle mode (0.2°) XRD pattern of MnO_x electrodes deposited for 2, 5, and 30 minutes followed by annealing at 400°C in air for 2h. **c**, Enlarged view of XRD pattern between $15\sim 20^\circ$ of XRD pattern of MnO_x highlighted in (b).

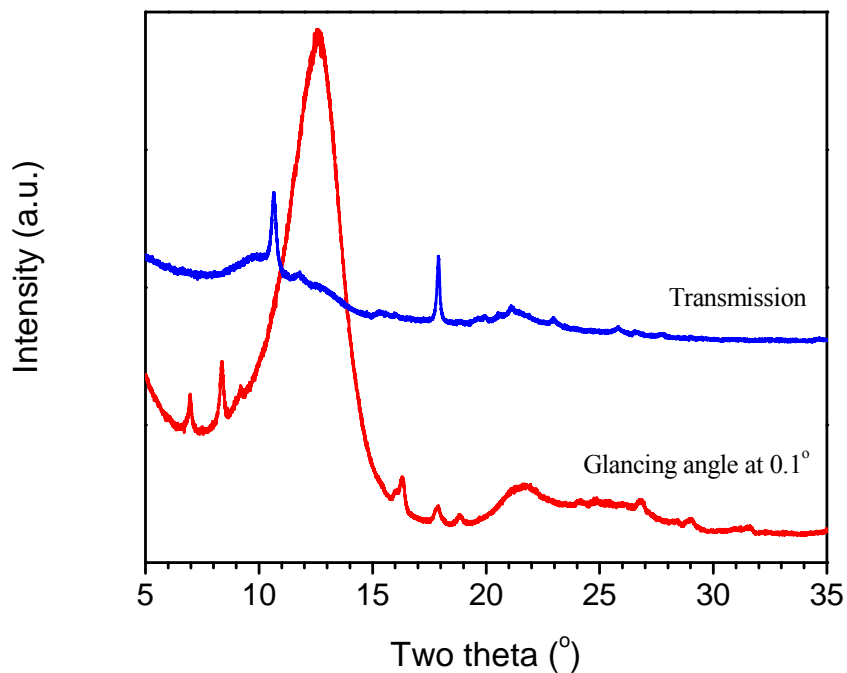


Fig. S9. Synchrotron-XRD patterns of MnO_x deposited for 2 minutes and annealed at 400°C in air for 2h. The differences between the patterns acquired in a transmission mode and a glancing angle (0.1°) mode suggest that the phases on the surface are very different from those in the bulk.

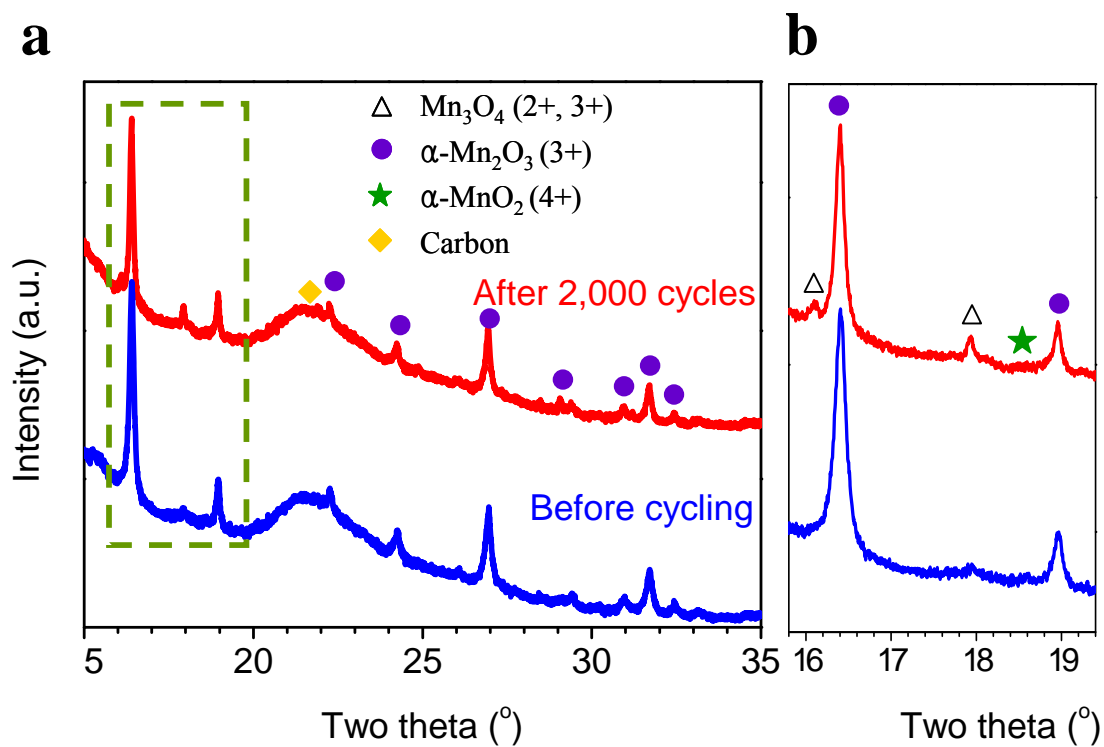


Fig. S10. a, Synchrotron X-ray diffraction (XRD) pattern (Transmission mode) of MnO_x electrodes before and after 2,000 cycles, **b**, Enlarged view of XRD pattern of MnO_x highlighted in (a). The mixed-phases (Mn_3O_4 , $\alpha\text{-Mn}_2\text{O}_3$ and $\alpha\text{-MnO}_2$) were retained after 2,000 cycles and the peak intensity of Mn_3O_4 slightly increased.

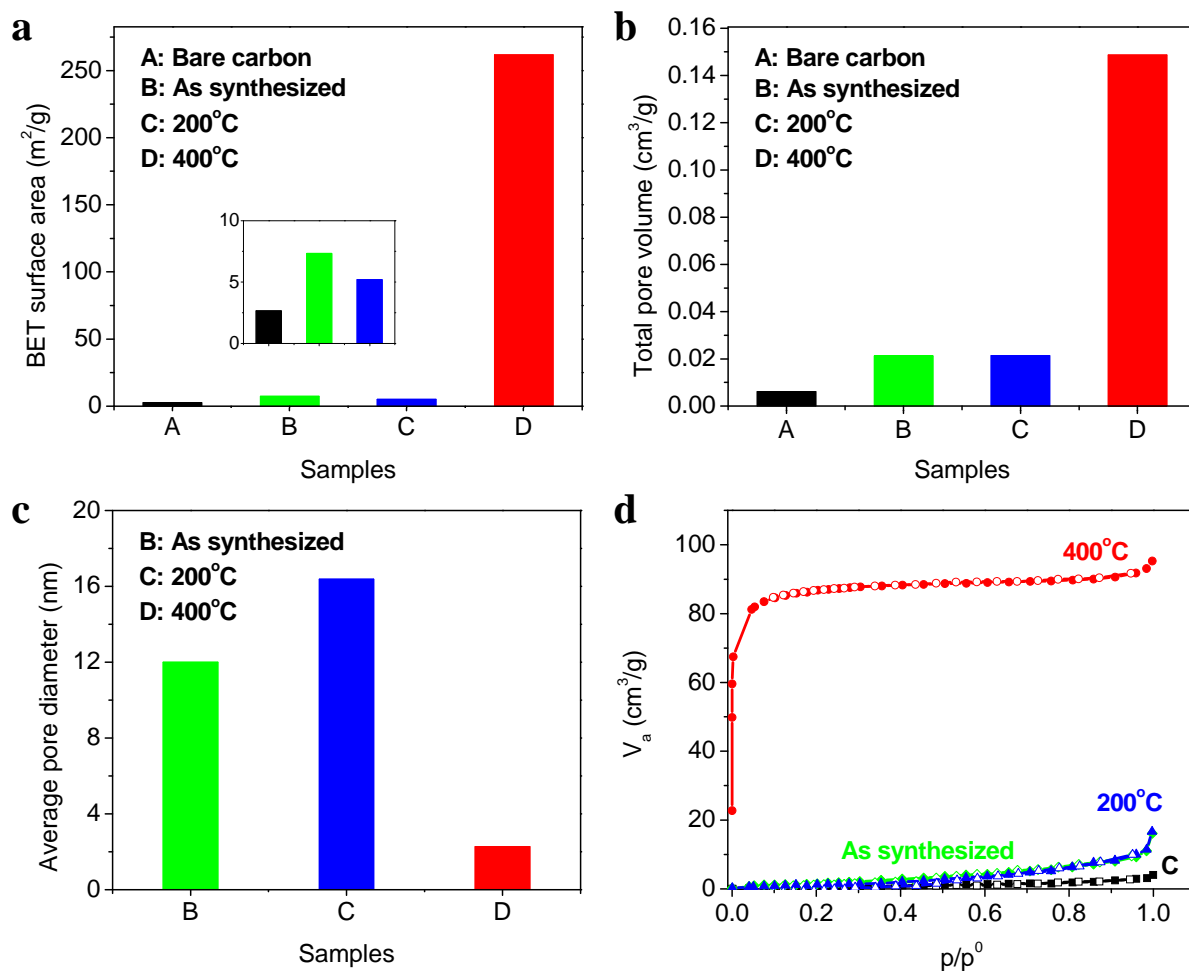


Fig. S11. Gas adsorption/desorption analysis of carbon, as-synthesized MnO_x sample, and MnO_x samples annealed at 200 and 400°C in air for 2h. **a**, BET surface areas. **b**, Total pore volumes. **c**, Average pore diameters. **d**, Nitrogen adsorption/desorption isotherm. These results suggest that the microstructure of the MnO_x underwent a dramatic rearrangement during annealing at 400°C in air for 2h, producing porous, nano-structured multi-valent MnO_x.

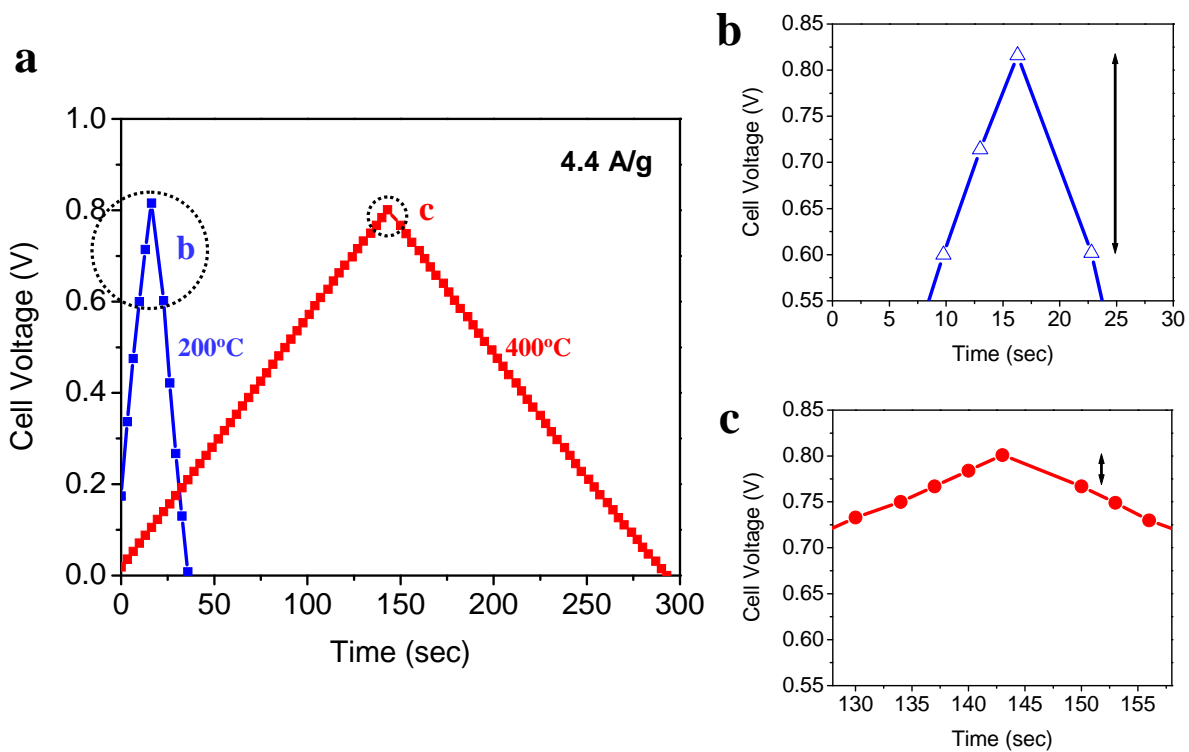


Fig. S12. a, Typical charge-discharge curves of symmetric pseudocapacitors constructed from amorphous MnO_2 and mixed-valent MnO_x electrodes at a constant current of 4.4 A/g. **b**, Enlarged views of iR drop of amorphous MnO_2 highlighted in (a). **c**, Enlarged views of iR drop of mixed-valent MnO_x electrodes highlighted in (a).

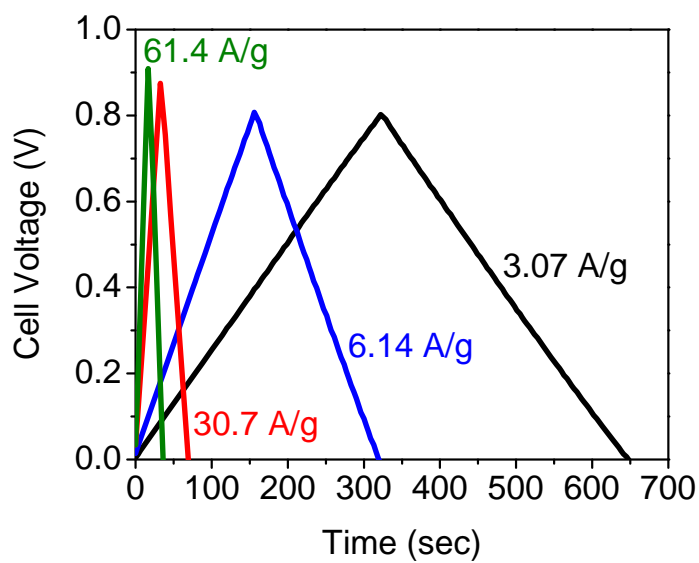


Fig. S13. Typical charge-discharge curves of symmetric pseudocapacitors constructed from mixed-valent MnO_x electrodes with Na^+ at different constant currents. The “linear” and symmetrical charge-discharge curves imply that surface reactions are highly reversible and very fast.

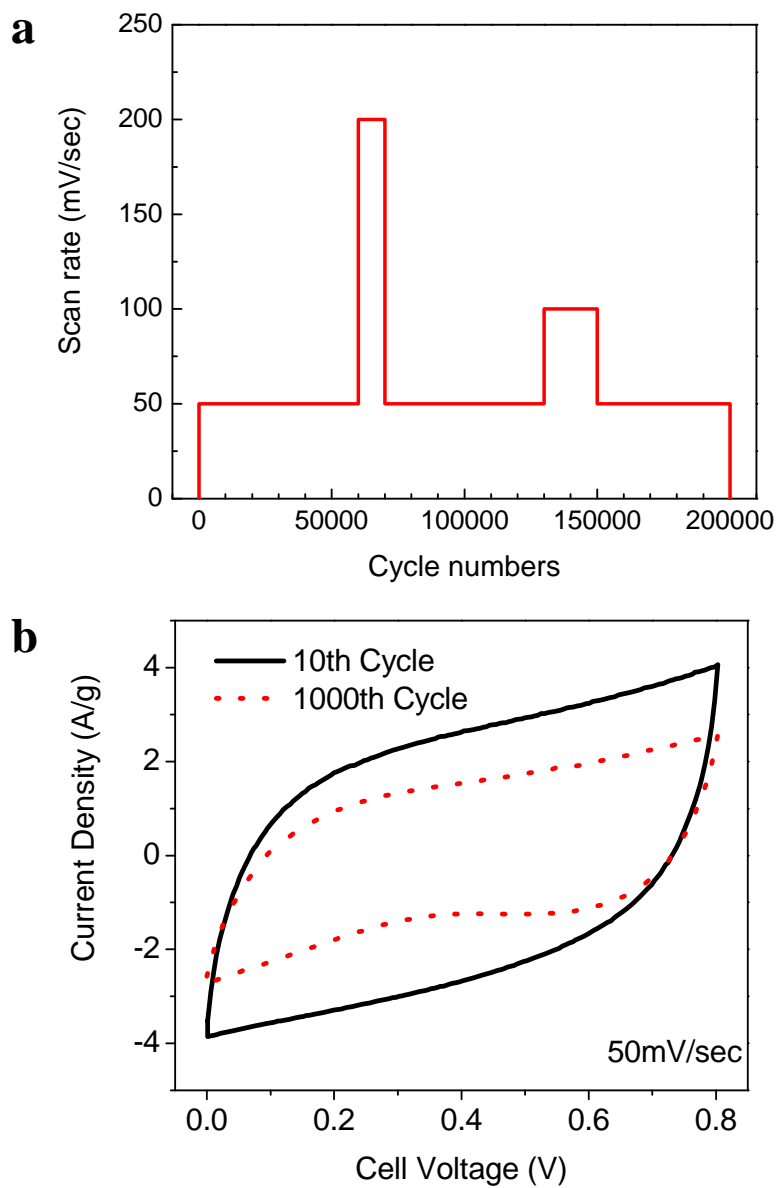


Fig. S14. a, Voltage scan rates used in the long-term cycling tests operated continuously for 200,000 cycles performed for a mixed-valent MnO_x electrode. **b,** Cyclic voltammograms of amorphous MnO₂ electrode: initial and after 1,000th cycle at a scan rate of 50 mV/sec showing notable degradation in performance during cycling.

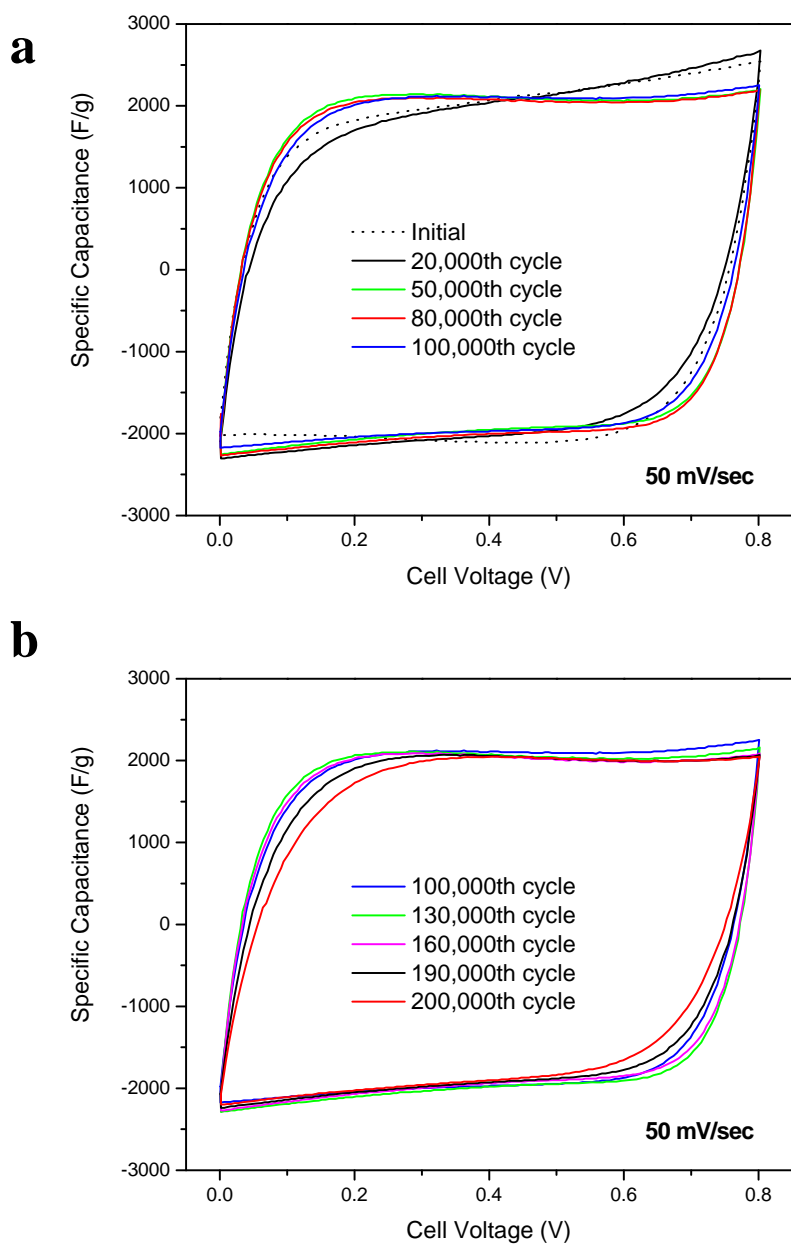


Fig. S15. Cyclic voltammograms of mixed-valent MnO_x electrode at different cycle numbers (**a**: initial~100,000th cycle, **b**: 100,000th~200,000th cycle) obtained at a scan rate of 50 mV/sec showing excellent cycling stability.

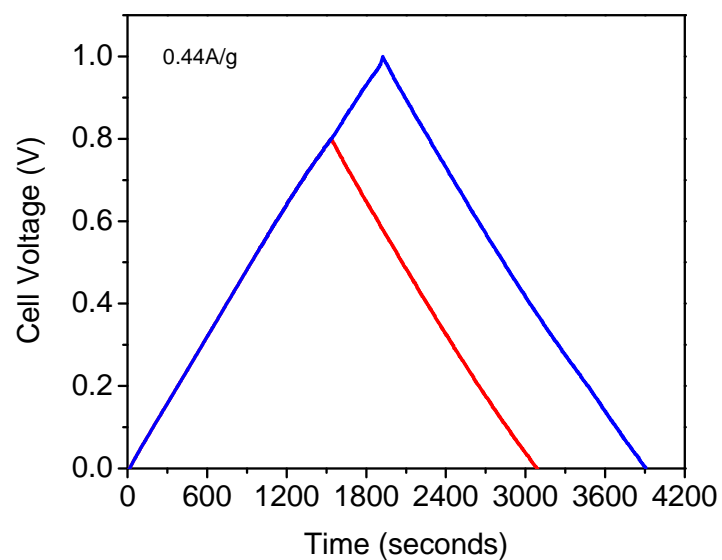


Fig. S16. Typical charge-discharge curves of symmetric pseudocapacitors constructed from mixed-valent MnO_x electrodes charged up to different voltage.

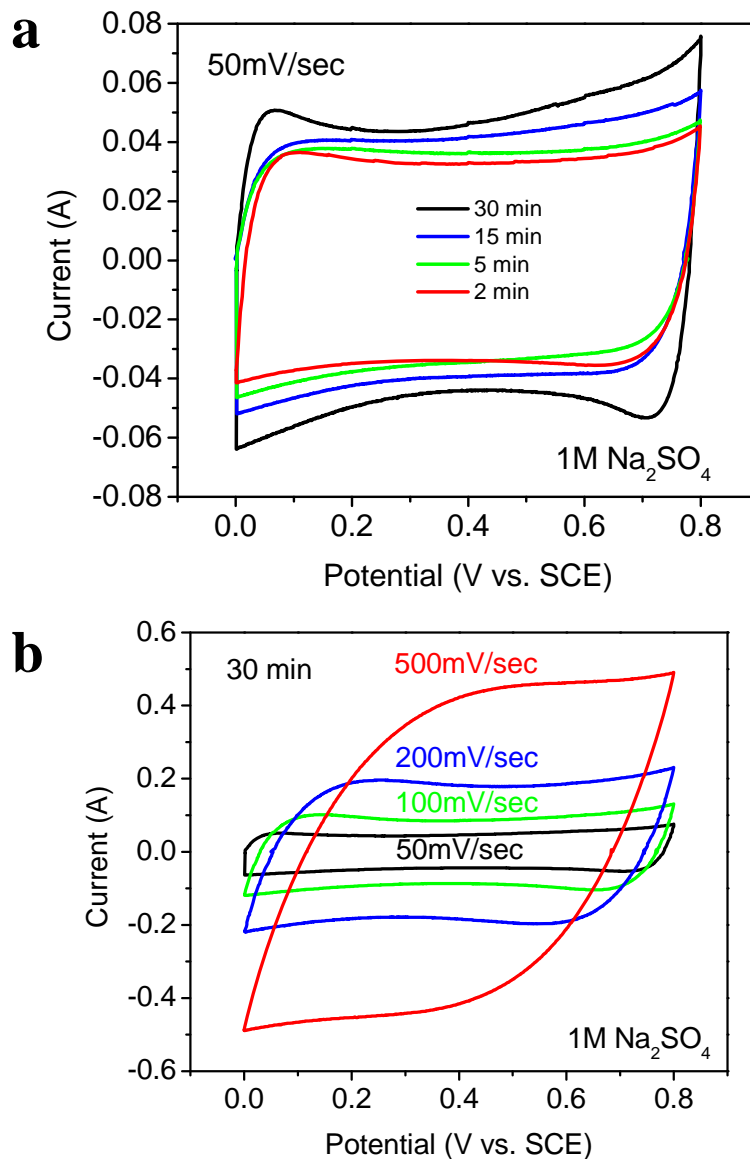


Fig. S17. a, Cyclic voltammograms of mixed-valent MnO_x/CFP composite electrodes with different loading amounts of manganese oxide tested in cells with a three-electrode configuration. **b,** Typical cyclic voltammograms of the MnO_x/CFP composite electrodes prepared by deposition of MnO_x for 30 minutes in 1M Na₂SO₄ solution measured at different scanning rates (50~500 mV/sec) using a 3-electrode configuration.

The potential was measured versus a Saturated Calomel Electrode (SCE) and the measured currents, not the normalized current with respect to the loading amount of MnO_x , are presented. The mixed-valent MnO_x /CFP electrode with different loadings of MnO_x all showed excellent “square-shape” cyclic voltammograms at 50 mV/sec in 1M Na_2SO_4 solution. The measured currents increased with the loading of MnO_x . For instance, at 0.4V (vs. SCE), the measured current of MnO_x deposited for 5, 15, and 30 minutes showed the 10.7%, 26.9% and 40.9% increase, compared to current from MnO_x deposited for 2 minutes. It is noted that even the sample with ~800 nm thick MnO_x coating (deposition of MnO_x for 30 minutes) showed symmetric shape and instant response upon the reversal of voltage, indicating that surface reactions are highly reversible and very fast as shown in Fig. S16 (b).

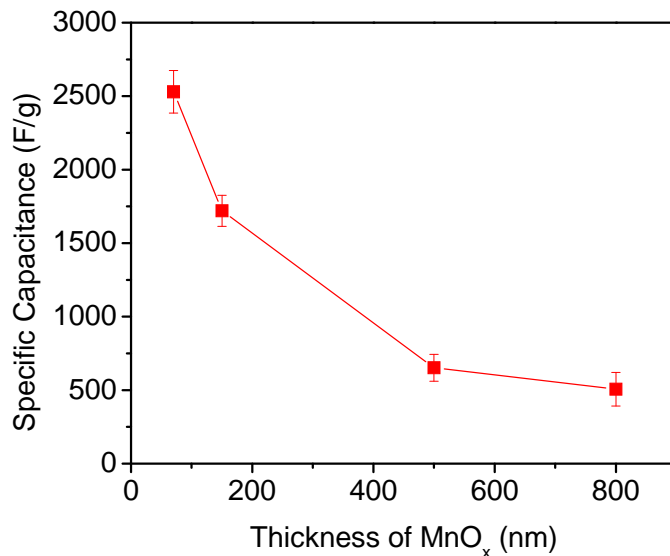


Fig. S18. Specific capacitance (of MnO_x) as a function of average thickness of mixed-valent MnO_x coating deposited for 2 to 30 minutes.

It is noted that the specific capacitance drops with the thickness of the MnO_x film (or loading), suggesting that only a thin film was fully utilized (or the nano-porous mixed-valent surface phases make dominating contributions to the observed capacitance). To increase the performance of electrochemical capacitors by increasing the MnO_x film thickness is, perhaps, fundamentally unattainable because the rate capability may ultimately diminish with film thickness. To increase practical energy density of electrochemical capacitors without penalizing high-rate capability, we believe that MnO_x coatings must be thin to offer the best possible power density. Therefore, one effective approach to increasing practical energy density (e.g. loading) without compromising the specific capacitance or rate capability is to reduce the diameter of the carbon fiber support (or use carbon nanofibers), thus increasing the surface area of CFP for conformal

coating of MnO_x . It is also noted that, due to the macro-porous feature of CFP and thin, conformal coating of MnO_x film, scale-up can be easily made by stacking the electrodes up to several layers without compromising excellent performance. We achieved similar performance (within 5%) with 4 layers stacked without any additional current collectors.

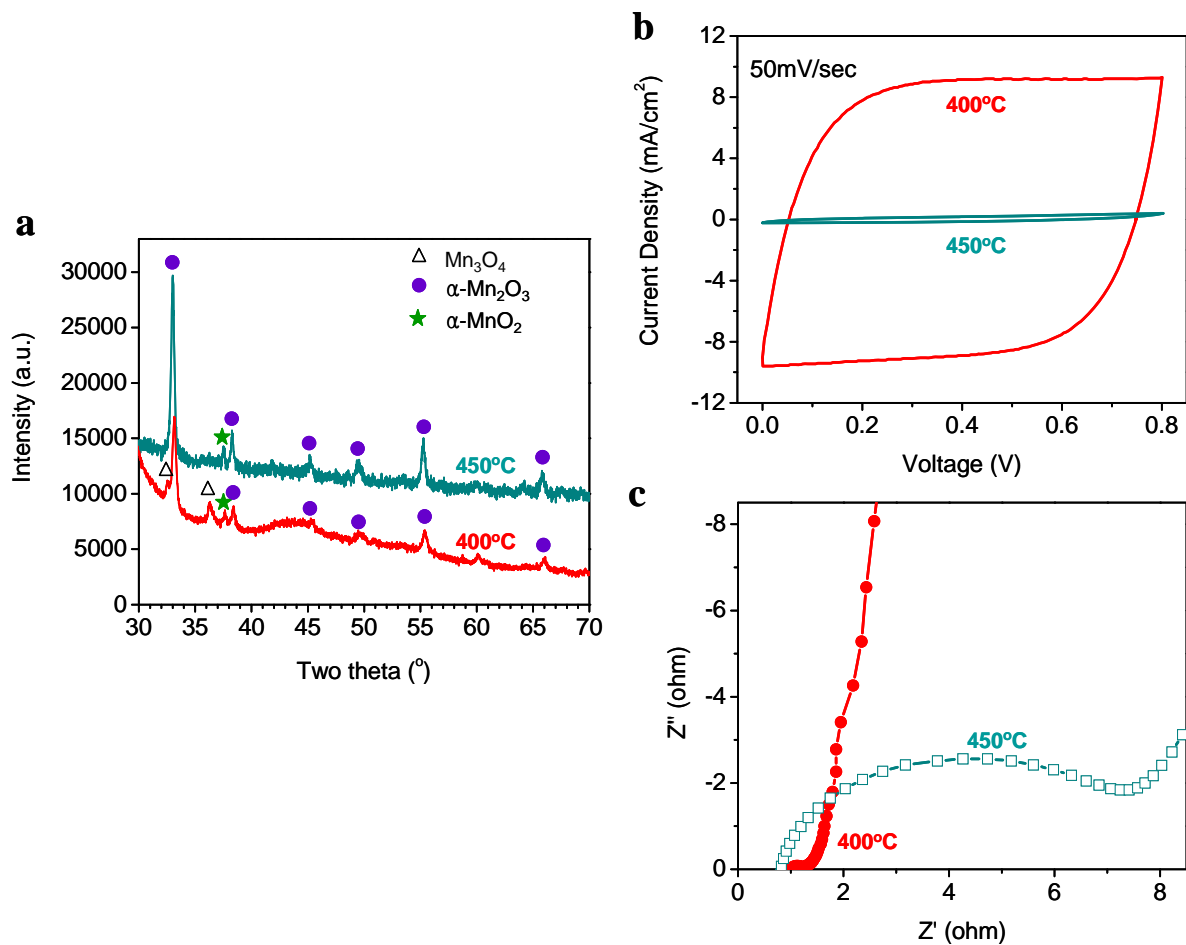


Fig. S19. **a**, Laboratory XRD pattern of MnO_x electrodes annealed at 400 and 450°C in air for 2h. **b**, Cyclic voltammograms measured at a scan rate of 50mV/sec of electrochemical capacitors constructed from electrodes annealed at 400 and 450°C in air for 2h. **c**, Electrochemical impedance spectra collected at open circuit voltage (OCV) under the influence of an ac voltage of 10 mV for. Fig. (a) shows the α-Mn₂O₃ peaks grew at 450°C while Mn₃O₄ peaks disappeared. It agrees well with our observation with *in-situ* Synchrotron XRD results. Interestingly, performance dropped significantly with increased charge transfer resistance as shown in Fig. (b) and (c).

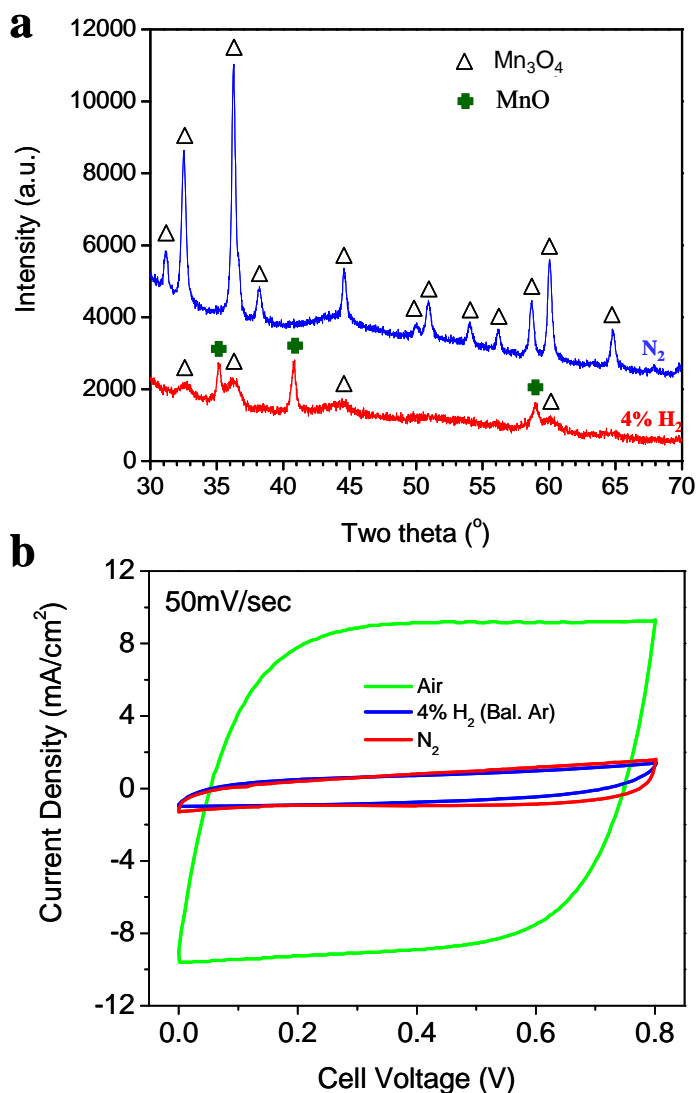


Fig. S20. a, Laboratory XRD pattern of MnO_x electrodes annealed at $400^{\circ}C$ in N_2 and 4% H_2 (balanced with Ar) for 2h. **b**, Cyclic voltammograms measured at a scan rate of 50mV/sec of electrochemical capacitors constructed from electrodes annealed at $400^{\circ}C$ in N_2 and 4% H_2 (balanced with Ar) for 2h. Fig. (a) shows that as-synthesized amorphous MnO_2 converted to pure Mn_3O_4 when annealed in N_2 and even reduced further to form MnO/Mn_3O_4 composite in 4% H_2 . The electrochemical performance of these electrodes dropped significantly compared to electrodes annealed in air at $400^{\circ}C$ for 2h as shown in Fig. (b).

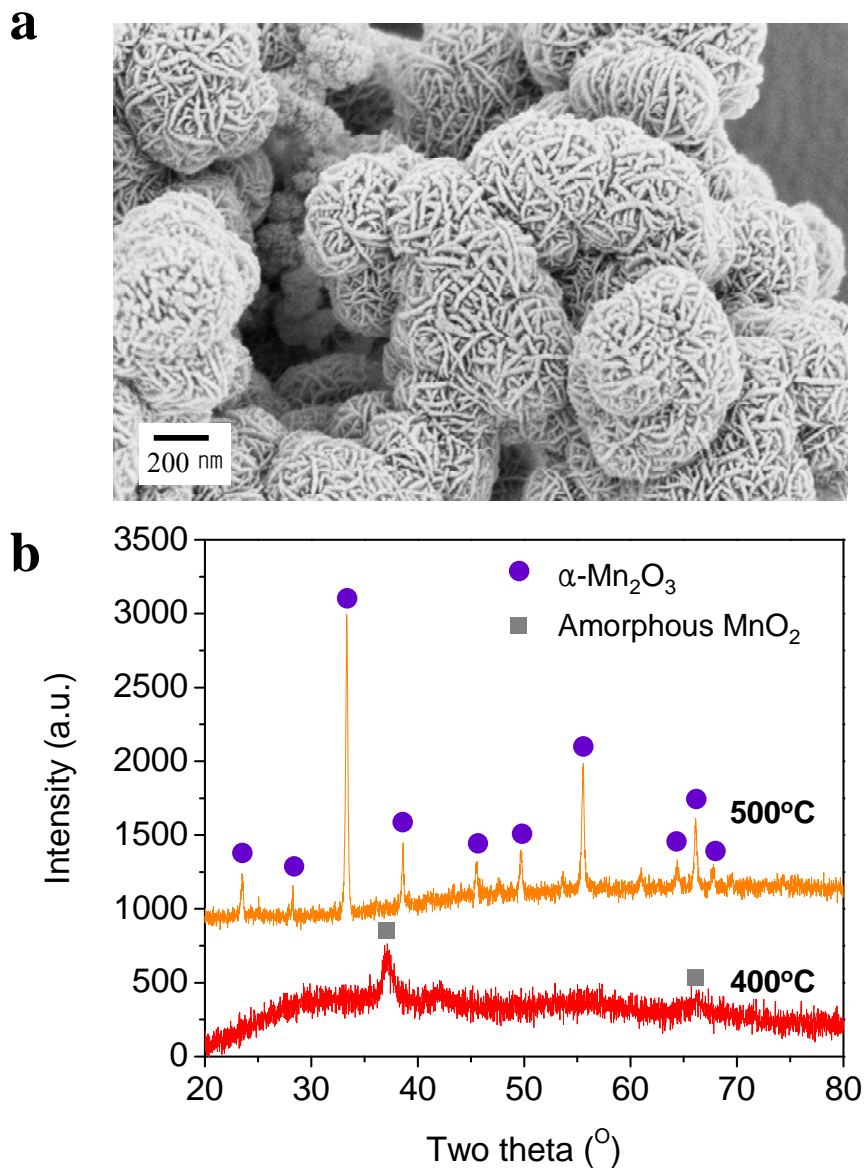


Fig. S21. a, SEM image of powder samples synthesized under the same condition ($KMnO_4$ as precursor in 2M H_2SO_4 solution at $75^\circ C$) without carbon fiber paper. **b**, Laboratory XRD patterns of the powder samples annealed at $400^\circ C$ and $500^\circ C$ in air for 2h without carbon fiber paper. Fig. (b) reveals that MnO_2 remained amorphous when annealed at $400^\circ C$ in air for 2 h without carbon, but transformed to crystalline α - Mn_2O_3 when annealed at $500^\circ C$ in air for 2 h without carbon.

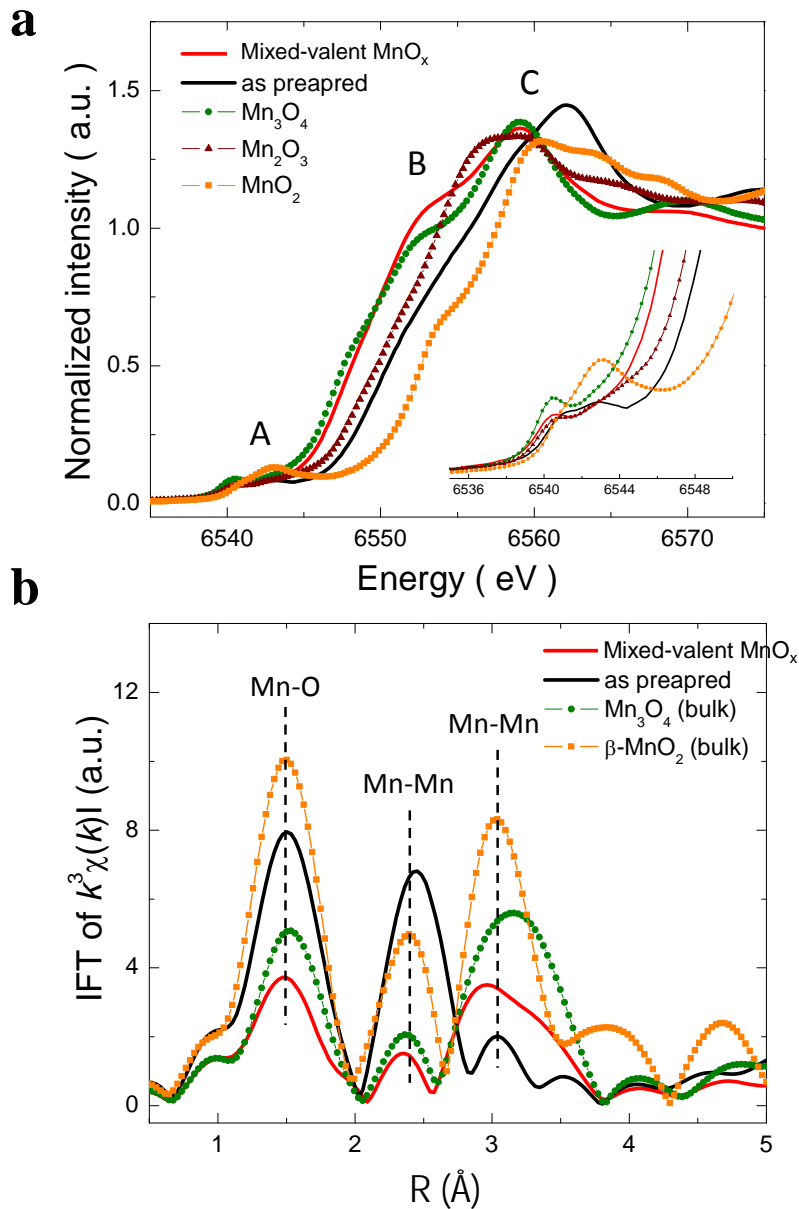


Fig. S22. a, Mn K-edge XANES spectra of the as-prepared and the mixed-valent MnO_x (heat-treated at 400°C in air for 2h) electrodes in comparison with the reference spectra for Mn₃O₄, Mn₂O₃ and MnO₂. Inset shows the enlargement of the pre-edge region A. **b**, Fourier transform (FT) magnitude of the k^3 weighted EXAFS spectra of the as-prepared and the mixed-valent MnO_x (heat-treated at 400°C in air for 2h) electrodes in comparison with the reference Mn₃O₄ and MnO₂ spectra. The FT was not phase corrected so that the actual bond length may be ca 0.2 ~ 0.4 Å longer.

We have performed both *ex-situ* and *in-situ* X-ray absorption spectroscopy (XAS) to explore the origin of the superior properties of this mixed-valent MnO_x material. XAS is a very useful tool to probe the changes in valence states (X-ray absorption near edge spectroscopy, XANES) and local coordination (extended X-ray absorption fine structure, EXAFS) of Mn cations in different structures during charge-discharge cycling.

Mn K-edge XANES spectra for the as-prepared (amorphous MnO_2) and the heat-treated (at 400°C in air for 2 h) MnO_x /CFP samples (deposited for 2 minutes) are shown in Fig. S22 in comparison with the reference spectra of several manganese oxides (Mn_3O_4 , Mn_2O_3 and MnO_2). Both the XANES and Fourier transform (FT) magnitude of the EXAFS spectrum reveal that the as-prepared manganese oxide has a layered K-birnessite (K_xMnO_2) type-structure with mixed $\text{Mn}^{3+}/\text{Mn}^{4+}$ ions. In contrast, the heat-treated (at 400°C in air for 2 h) manganese oxide has an average electronic and local structure similar to those of Mn_3O_4 . It agrees very well with our synchrotron-based XRD analyses, which showed that the bulk phase of the heat-treated, mixed-valent MnO_x (deposited for 2 minutes) was Mn_3O_4 . Average Mn valances for the as-prepared (amorphous MnO_2) and the heat-treated (mixed-valent MnO_x) samples were estimated to be ~ 3.3 and ~ 2.7 by comparing the XANES edge positions at half height with those for the reference Mn oxides.

The most interesting difference between the as-prepared and the heat-treated sample is in the main edge absorption feature B, which is assigned to a shakedown process involving the $1s$ to $4p$ transition followed by ligand-to-metal charge transfer (LMCT)^{9, 10}, or in other words, a hole state redistribution toward the oxygen sites, as an indicator for the degree of covalent character by the $\text{Mn}(3d)\text{-O}(2p)$ bond. Feature B is not observed in

the as-prepared sample but very strong for the heat-treated sample with even higher intensity than the Mn_3O_4 reference, indicating increased covalent bond character between the Mn(3d)-O(2p) bond in the heat-treated material, which is quite important and will be further discussed in the *in-situ* XANES results later. It should be noted that the heat-treated sample is also quite different from the Mn_3O_4 sample in the pre-edge feature A, which is partially allowed because of electric quadrupole coupling and/or 3d-4p orbital mixing arising from the non-centrosymmetric environment in the Mn-O coordination. The weaker intensity in feature A shows that the heat-treated sample has less tetrahedral sited Mn than the bulk Mn_3O_4 reference, which is further supported by the Fourier transformed EXAFS in Fig. S22 (B), indicating that significant structural differences exist between heat-treated sample (i.e., mixed-valent MnO_x) and the bulk Mn_3O_4 reference.

The Fourier transformed magnitude of EXAFS spectrum for the heat-treated sample (mixed-valent MnO_x) shows much smaller intensity in the first three shells located around 1.5, 2.2 and 3.1 Å corresponding to Mn-O, Mn-Mn, and overlapped Mn-O and Mn-Mn contribution in the Mn_3O_4 structure. The decreased FT peak intensity could be due to the Mn defects in the Mn-O_4 tetrahedral sites of Mn_3O_4 structure and broad distribution of Mn-O and Mn-Mn bond lengths due to the mixed Mn valence character of the mixed-valent MnO_x . In addition, the slightly shorter Mn-O distance of the mixed-valent MnO_x than Mn_3O_4 is due to either the increased covalent bonding character between Mn (3d) and O (2p) orbitals or the existence of Mn-O coordinations in the Mn_2O_3 and MnO_2 like environments in line with the mixed valence state of Mn ions in the mixed-valent MnO_x .

These unique XANES and EXAFS data implies that the mixed-valent MnO_x (the heat-treated sample) has unique structure with totally different Mn cation site distribution and electronic structure (e.g. covalent bond character between Mn and O ions) than all of the bulk reference manganese oxides (such as Mn_3O_4 , Mn_2O_3 , and MnO_2) due to the mixed valence state of manganese ions (e.g., Mn^{2+} , Mn^{3+} and Mn^{4+}) created during the heat-treatment process.

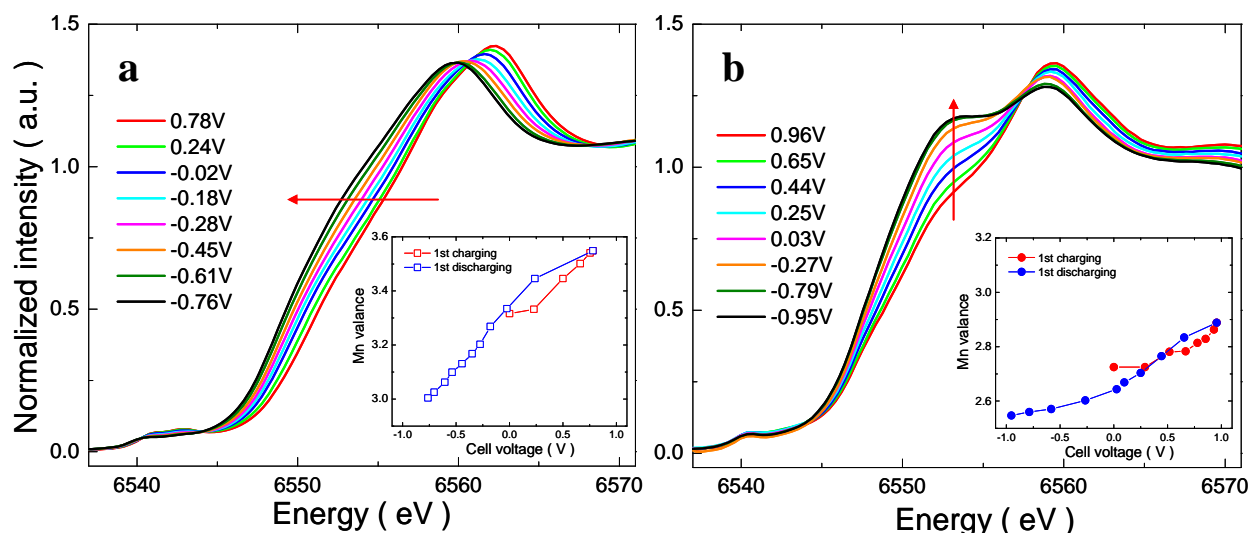


Fig. S23. XANES spectra of the positive electrodes in the *in-situ* (symmetric) cell for **a**, the as-prepared and **b**, mixed-valent MnO_x electrode during discharge in 1M Na_2SO_4 electrolyte.

To directly correlate the oxidation state of Mn ions with the capacitance or electrochemical state of the electrode in a capacitor, we performed *in-situ* Mn K-edge fluorescence X-ray absorption spectroscopy (XAS) to probe the local atomic and electronic structural change of the as-synthesized sample (amorphous MnO_2) and the heat-treated sample (mixed-valent MnO_x) as a function of the applied potential in 1M Na_2SO_4 . Fig. S23 shows the *in-situ* XANES spectra for the as-prepared and the heat-treated electrodes during the 1st discharge (positive electrode in the *in-situ* cell). The voltage window for the cell using the as-prepared electrodes was cycled in a narrower (+0.8 to -0.8 V) range than that (+1.0 to -1.0V) for the cell using the heat-treated electrodes, due to the oxygen evolution reaction at voltage over +0.8V. The cells were

discharged below 0.0V to monitor full ranges of the valence state changes at the positive electrodes. For the as-prepared sample, the XANES spectra showed entire edge shift towards the lower energy position in a continuous manner during the discharge process, revealing that the charge storage mechanism is mostly attributed to the $\text{Mn}^{3+}/\text{Mn}^{4+}$ redox reactions on Mn sites. This is typical for most of the Mn K-edge XANES changes of manganese oxides for pseudocapacitors, which agrees well with the common belief that the charge compensation for the incorporation/extraction of cations into the MnO_2 occurs in the Mn site by the redox reactions between Mn^{3+} and Mn^{4+} ions.

However, we have noticed that, quite interestingly, the XANES spectra for the heat-treated sample (mixed-valent MnO_x) showed completely different spectral feature changes during the discharge, which have never before been reported. Shown in Fig. S23 (b), slight edge shift towards lower energy was observed, indicating the decrease of average oxidation state of Mn ions. However, there is no obvious entire edge shift during discharge as observed for the as-prepared electrode. Instead, we observed a unique evolution of the B peak, which is related to the ligand-to-metal charge transfer process. The increased B peak intensity indicates the increased degree of covalent character of Mn(3d)-O(2p) bonding during discharge. Therefore, the unique Mn K-edge change in the form of increasing B feature clearly shows that a large portion of the charge compensation during discharge might be originated from the hole state redistribution towards the oxygen sites, rather than just the decreasing number of Mn^{4+} at the Mn sites (as in the case of the as-prepared sample). Although small intensity change of B feature in XANES spectra during charge-discharge had been reported in the literature^{11, 12} for transition metals such as Co and Mn, it has never before been observed that this spectral

change plays a dominating role over the edge shift. The role of oxygen anions in transition metal oxides for charge compensation was previously argued for lithium battery electrodes. Aydinol et al. showed that, in their *ab initio* study, more charge can be transferred to the oxygen anions upon intercalation of lithium ions than to the metal cations in the oxide¹³. In our *in-situ* synchrotron XAS experiments, we have monitored that the charge compensation for the electron exchange can be achieved at oxygen site as well as Mn site, which has never before been reported for pseudocapacitor electrodes. The unique atomic and electronic structure of the nanostructured, mixed-valent MnO_x may allow this additional charge compensation mechanism which is not observed in MnO_2 .

As shown in the inset of Fig. S23, although the heat-treated sample of mixed-valent MnO_x showed much higher capacitance than the as-prepared material, the average Mn valance change within the 0.8 to 0.0V window calculated from the edge shift is estimated to be $\sim 0.3e$ which is similar for the as-prepared material within the 0.8 to 0.0 V window. The observed valence change of Mn ion cannot account for the large pseudocapacitance observed experimentally. This result provides a further support to the hypothesis that the large portion of the charge compensation during discharge might be originated from the hole state redistribution towards oxygen sites. If the oxygen anions in a metal oxide can indeed provide additional charge composition mechanism, it will open a new approach to design and synthesis of new electrode materials with greater capacity for supercapacitors and batteries.

DFT-based calculation also support the evidence that the observed capacitances of our nanoporous multi-phase, multi-valent MnO_x are due to the amount of charge

accumulated at O sites and surfaces. Our state-of-the-art DFT+U calculations indeed show that, while Mn cations act as attractors of negative charge, the surface and O sub-network constitute regions where the excess negative charge can be further deposited. In Mn_3O_4 , charge accumulation at O centers and surface seems to result from the delicate balance of the geometrical features of the crystal and the electronic coupling between 3d and 2p states of the Mn and O ions. A deeper understanding of the delicate competition between structure, electronic properties, and surface effects leading to the charge storage ability of manganese oxides is needed and further computations are at present in progress to elucidate these critical issues.

Supplementary References

1. Chmiola, J.; Yushin, G.; Gogotsi, Y.; Portet, C.; Simon, P.; Taberna, P. L. *Science* **2006**, 313, (5794), 1760-1763.
2. Korenblit, Y.; Rose, M.; Kockrick, E.; Borchardt, L.; Kvit, A.; Kaskel, S.; Yushin, G. *ACS Nano* **2010**, 4, (3), 1337-1344.
3. Kresse, G.; Furthmuller, J. *Physical Review B* **1996**, 54, (16), 11169-11186.
4. Kresse, G.; Joubert, D. *Physical Review B* **1999**, 59, (3), 1758-1775.
5. Perdew, J. P.; Burke, K.; Ernzerhof, M. *Physical Review Letters* **1996**, 77, (18), 3865-3868.
6. Dudarev, S. L.; Botton, G. A.; Savrasov, S. Y.; Humphreys, C. J.; Sutton, A. P. *Physical Review B* **1998**, 57, (3), 1505-1509.
7. Franchini, C.; Podloucky, R.; Paier, J.; Marsman, M.; Kresse, G. *Physical Review B* **2007**, 75, (19).
8. Bader, R. F. W., *Atoms in Molecules - A Quantum Theory*. Oxford University Press: 1990.
9. Kim, M. G.; Yo, C. H. *J. Phys. Chem. B* **1999**, 103, (31), 6457-6465.
10. Horne, C. R.; Bergmann, U.; Grush, M. M.; Perera, R. C. C.; Ederer, D. L.; Callcott, T. A.; Cairns, E. J.; Cramer, S. P. *J. Phys. Chem. B* **2000**, 104, (41), 9587-9596.
11. Yoon, W. S.; Balasubramanian, M.; Chung, K. Y.; Yang, X. Q.; McBreen, J.; Grey, C. P.; Fischer, D. A. *J. Am. Chem. Soc.* **2005**, 127, (49), 17479-17487.
12. Kim, M. G.; Shin, H. J.; Kim, J. H.; Park, S. H.; Sun, Y. K. *J. Electrochem. Soc.* **2005**, 152, (7), A1320-A1328.
13. Aydinol, M. K.; Kohan, A. F.; Ceder, G.; Cho, K.; Joannopoulos, J. *Physical Review B* **1997**, 56, (3), 1354-1365.